

1 **Microphysical properties of various precipitation systems worldwide**
2 **classified via objective methods based on dual-frequency precipitation**
3 **radar observations**

4 Yujia Zhang^{1,2} Xiaodong Zhang^{1,2}, Xiang Ni^{1,2}

5 ¹Chongqing Jinfo Mountain Karst Ecosystem National Observation and Research Station, School of Geographical Sciences,
6 Southwest University, Chongqing, China

7 ²Chongqing Engineering Research Center for Remote Sensing Big Data Application, School of Geographical Sciences,
8 Southwest University, Chongqing, China

9 *Correspondence to:* Xiang Ni (nixiang@swu.edu.cn)

10

11 **Abstract.** Microphysical properties play crucial roles in physical processes related to the development of precipitation. In this
12 study, Global Precipitation Measurement (GPM) dual-frequency precipitation radar (DPR) data were processed to demonstrate
13 the microphysical properties of different precipitation systems (PSs) that are objectively classified with the k-means clustering
14 algorithm. Four types of regular/non-extreme PS (high-latitude shallow PS, subtropical shallow PS, moderate PS, deep PS)
15 and four types of extreme PS (extreme deep PS, strong PS, extreme strong PS, and marine extreme PS) were recognized. These
16 eight types of PS exhibit differences in spatial-temporal features and convection characteristics, such as storm height, rain
17 intensity, and vertical structures. For example, the extreme strong PS, with the highest radar echo top and ~~the~~ largest mean
18 mass-weighted mean diameter (D_m), ~~the extreme strong PS~~ mainly locate over tropical continent, ~~while-whereas the~~ high-
19 latitude shallow PS have the least precipitation rate and mean normalized intercept parameter (N_w) values. The relationships
20 between convection features and microphysical properties also vary among the eight types of PSs. For extreme PS, maximum
21 precipitation rate near the surface generally exceeds 100 mm h^{-1} and balanced breakup and coalescence processes play a
22 dominant role compared with non-extreme PS. In contrary, the coalescence processes dominate near the surface in two types
23 of shallow PS. These results highlight the diversity of global precipitation microphysics and emphasize the necessity of global
24 studies to increase the understanding of precipitation processes.

25

26 1. Introduction

27 The microphysical characteristics of precipitation provide crucial information for describing precipitation. The deficiency of
28 precipitation microphysical parameterization schemes is a significant factor contributing to precipitation errors in weather and
29 climate models (Snook and Xue, 2008). Accurately obtaining ~~spatiotemporal spatial and temporal distributions and~~ variations
30 in precipitation microphysical parameters is essential for understanding the physical processes of precipitation, increasing the
31 accuracy of quantitative precipitation estimation ~~(QPE)~~, and evaluating microphysical parameterizations in models (Chen et
32 al., 2011; Zhang et al., 2023). Currently, observations and characteristics of precipitation microphysics at the global scale
33 remain lacking because of the limited number of observation approaches.

34
35 The drop size distribution (DSD) is a typical metric for depicting precipitation microphysics. DSD features can be derived
36 from observations obtained via disdrometers, ground-based radar instruments, and space-based radar instruments. In radar
37 instruments, the interaction of electromagnetic waves with hydrometeors is used to retrieve DSD parameters (Marzuki et al.,
38 2023), whereas disdrometers measure raindrop counts to directly obtain DSDs at the surface. Disdrometers provide only point
39 measurements at specific levels and cannot measure the vertical structure of DSDs. Moreover, disdrometers have not been
40 deployed globally, especially over the ocean. Although ground-based radar instruments can measure the three-dimensional
41 structure of precipitation, they can only be used in limited areas, and their observation accuracy is significantly affected by the
42 terrain conditions within the observation area (Dai et al., 2020). In contrast, space-based radar instruments can provide the
43 vertical structures of DSD parameters worldwide. This study focused on the microphysical characteristics of various
44 precipitation systems (PSs) worldwide. Compared with other instruments, space-based radar instruments are the most suitable
45 for researching global precipitation microphysics.

46
47 In 1997, the Tropical Rainfall Measuring Mission (TRMM) satellite was launched by the National Aeronautics and Space
48 Administration (NASA) and the Japan Aerospace Exploration Agency (JAXA). The precipitation radar (PR), which operates
49 in the Ku-band (13.8 GHz), was carried by the TRMM (Iguchi et al., 2000). This marked the beginning of the observation of
50 precipitation microphysics via space-based radar instruments. Notably, DSD parameters were retrieved from the radar
51 reflectivity measured by the PR with the assumption that the DSD can be characterized by the diameter parameter itself (Iguchi
52 et al., 2000). As a result, the DSDs obtained via retrieval exhibited large errors. In 2014, NASA and JAXA successfully
53 launched the Global Precipitation Measurement (GPM) Core Observatory (GPM-CO). The GPM-CO carried the first
54 spaceborne dual-frequency precipitation radar (DPR) system, operating in the Ku and Ka bands (13.6 and 35.5 GHz,
55 respectively) (Skofronick-Jackson et al., 2017). ~~The differential scattering during rainfall at these two frequencies is directly~~
56 ~~related to the size of raindrops (Gatlin et al., 2020).~~ Via the use of this characteristic, ~~mean mass-weighted mean diameter~~
57 ~~(D_m) D_m and mean normalized intercept parameter (N_w) N_w~~ can be retrieved. The retrieved DSD parameters have been verified
58 with ground-based observations and are better than those obtained via the TRMM PR algorithm (Sun et al., 2020). In addition,

59 validation studies have confirmed the feasibility of using DPR observations for DSD parameter analysis (D'Adderio et al.,
60 2018; Peinó et al., 2024). Peinó et al. (2024) used observational data from seven Parsivel disdrometers across different
61 topographic zones in the western Mediterranean to validate GPM DSD products. They reported that the GPM DPR products
62 effectively captured the variations in DSDs observed under different rainfall intensities. Therefore, GPM DSD products have
63 been widely employed to investigate the microphysical characteristics of precipitation in the literature (Wen et al., 2024, 2023).
64

65 However, previous studies involving GPM DSD products have focused mainly on specific locations or weather systems. For
66 example, Li et al. (2024) studied the vertical structure and DSD characteristics of different precipitation types during the rainy
67 season over South China and reported that the precipitation type and intensity affect the DSD parameters. In their study, under
68 the same precipitation intensity, shallow convective precipitation exhibited the smallest D_m and largest N_w values, whereas
69 deep convective precipitation exhibited the opposite phenomenon. Additionally, regarding stratiform precipitation, for PR
70 $\text{Precipitation Rate} > 3.5 \text{ mm h}^{-1}$, D_m slightly increased, and in regard to shallow convective precipitation, D_m remained at
71 approximately 1.3 mm for $\text{Precipitation Rate PR} > 2 \text{ mm h}^{-1}$. Similarly, Wen et al. (2023) analyzed the seasonal variations in
72 the vertical structure of precipitation microphysics in East China. They reported that the spatial distributions of D_m and N_w
73 demonstrate obvious seasonal variations and that there are more small raindrops in convective precipitation in autumn and
74 winter than during the other seasons. These studies revealed the variations in microphysical characteristics across different
75 seasons and rainfall types. Additionally, regarding weather conditions, regional variations in the precipitation characteristics
76 of tropical cyclones (TCs) have been investigated over the North Indian Ocean (Kumar et al., 2023). Research has revealed
77 that the nature of microphysical processes largely influences the growth of droplets in convective and stratiform rain. Wu et
78 al. (2022) investigated the DSD characteristics of record-breaking Typhoon In-Fa (~~2021~~). Their findings revealed significant
79 internal and regional differences in the microphysical characteristics of typhoon precipitation. When different precipitation
80 types during Typhoon In-Fa were compared, convective precipitation (N_w values ranging from 3.80 to 3.96 $\text{m}^{-3} \text{ mm}^{-1}$)
81 exhibited higher raindrop concentrations than did stratiform precipitation (N_w values ranging from 3.40 to 3.50 $\text{m}^{-3} \text{ mm}^{-1}$).
82 Additionally, convective precipitation during Typhoon In-Fa indicated a greater (lower) raindrop concentration than that
83 during Typhoon Taiwan (Hainan), while the raindrop diameter was smaller than those during both Typhoons Taiwan and
84 Hainan. These studies primarily focused on the microphysical process and structure of various weather conditions, which
85 provided insight into the formation process of precipitation. At present, there are few studies on the microphysical
86 characteristics of large-scale and global PSs. On the one hand, as mentioned above, the DSD is influenced by numerous factors,
87 such as precipitation type and season. There may be multiple precipitation types and DSDs in one area. On the other hand, few
88 DSD datasets covering the whole world are available. Dolan et al. (2018) used twelve disdrometer datasets across three
89 latitudinal zones—high-latitude, midlatitude, and low-latitude zones—to analyze DSD spatial variability. They reported that
90 the DSD varies with latitude. At low latitudes, moderate D_m values (1.5–2 mm) and large $\log_{10}(N_w)$ values ($> 4 \text{ m}^{-3} \text{ mm}^{-1}$)
91 dominated. At midlatitudes, high D_m values and small N_w values dominated. At high latitudes, low D_m and large N_w values
92 prevailed. Although the dataset covered a wide range of precipitation regimes, it could not capture all rain regimes. Moreover,

93 a regional DSD dataset cannot represent the DSD within a given latitudinal band because of the limitations of disdrometers.
94 Hence, in this study, GPM DSD products were employed to investigate the microphysical characteristics of PSs at global
95 scales. Additionally, Zhang and Wang (2021) used the latest Integrated Multi-satellite Retrievals for Global Precipitation
96 Measurement (IMERG) data to analyze the spatiotemporal variations of precipitation systems at different scales, revealing
97 significant differences in precipitation characteristics across regions. However, IMERG data can only depict the horizontal
98 distribution and evolution of precipitation systems, but cannot capture the three-dimensional structure of storms.

99

100 This study aimed to classify different PSs on the basis of DPR observations via machine learning and to analyze the
101 microphysical characteristics of different types of PSs ~~if PSs~~. The results could address regional DSD variability and increase
102 our understanding of the microphysical processes of different types of PSs. This study is organized in four sections. Section 2
103 provides detailed descriptions of the GPM data and machine learning models applied in this study. The main results are
104 presented in Section 3, and finally, a summary is given in Section 4.

105 2. Data and methods

106 2.1. Data

107 GPM observations cover the range from 65° S to 65° N (Hou et al., 2014; Tapiador et al., 2012). The GPM DPR operates in
108 the Ka and Ku bands, with a spatial resolution of approximately 5×5 km². The scanning of DPR is cross-track and has three
109 scan patterns: normal scanning (NS), matching scanning (MS), and high sensitivity scanning (HS) (Das et al., 2022). Since the
110 scanning pattern of the Ka-band was changed in 2018 (Awaka et al., 2021), the GPM 2A DPR (version 7) products considered
111 the changes in the Ka-band scan pattern with a more accurate precipitation estimation algorithm. The product formats in
112 version 7 have been changed from the original three types to two types: FS-Full sScan and High Sensitivity scanHS. The FS
113 Full scan product exhibits a new format and is defined as a full-scan dual-frequency product with a 125-m vertical range
114 resolution-distance resolution. Compared with previous algorithms, the FS-Full Scan mode makes it possible for the first time
115 to process a full-scan band of approximately 245 km in dual-band mode (Awaka et al., 2021). Therefore, the FS
116 type observations from the Full scan ~~were~~ was adopted in this study.

117

118 In this study, five years (2018–2022) of 2A DPR products (version 7) were employed. The parameters used in this machine
119 learning model include DSD parameters (D_m and N_w), near-surface precipitation rate (mm h^{-1}), attenuation-corrected radar
120 reflectivity (dBZ), reflectivity near the surface (Z_{surf}), and typeprecip (stratiform-and-or convective-precipitation pixels are
121 distinguished-by-the-typeprecip-parameter), and airTemperature. Detailed descriptions of the generation and retrieval of these
122 parameters can be found in Iguchi et al. (2021). The precipitation type helps distinguish between stratiform and convective
123 precipitation pixels, while air temperature is used to separates snow from rain. ~~(this parameter can be used to distinguish~~
124 ~~between snow and rain).~~

125 2.2. Precipitation system (PS)

126 This paper presents a method based on the connected domain principle for identifying PSs, similar to those contained in the
127 widely used TRMM/GPM Precipitation Feature dataset (Liu et al., 2008, 2020). First, pixels with precipitation no less than
128 0.1 mm h⁻¹ are derived from DPR orbit data. Then, neighboring precipitation pixels, including diagonally adjacent precipitation
129 pixels Similar to the Precipitation Feature dataset (Liu et al., 2008), neighboring precipitation pixels, with a minimum
130 precipitation rate of 0.1 mm h⁻¹, are grouped into a PS together as a PS. Each PS is required to have a minimum of four
131 precipitation pixels.

132
133 The DPR ~~can observe the~~ provides three-dimensional structure of precipitation and DPR products include radar reflectivity
134 parameters and retrieved DSD parameters from 0 to 22 km with a range resolution of 125 m, ~~resulting in a total of 176 layers~~
135 ~~of data.~~ Consequently, for each PS type, DSD and radar reflectivity parameters such as the maximum and average values of
136 each layer were calculated. The average D_m and N_w profiles were used for each PS, and if the profiles of the maximum D_m and
137 N_w values in each layer were involved, MAX- D_m and MAX- N_w , respectively, were used. Given the potential relationships of
138 the convective intensity with microphysical parameters, Z_e in the product was employed to calculate several convection
139 indicators. These include the maximum 20/30/40 dBZ echo top height (MAXHT20/30/40) for each type of PS (Liu, 2011; Liu
140 et al., 2020; Ni et al., 2019; Roy et al., 2020), the echo top height of the PS (H_{top}) (Arulraj and Barros, 2021), and other
141 convective parameters. To ~~describe PS conditions~~ characterize the conditions of the PS, several additional features were
142 calculated, ~~such as including~~ the maximum precipitation rate near the surface (~~the~~ maximum precipitation rate of the
143 precipitation pixels included in the PS) and ~~the~~ precipitation area (the number of precipitation pixels contained in the PS). For
144 the stratiform, convective, land, and oceanic percentages ~~these attributes,~~ the corresponding pixel fractions among each
145 individual PS were first calculated for each individual PS. These fractions were then averaged across all PSs within a given
146 cluster to represent the cluster-level characteristics. Considering that the GPM satellite exhibits a higher observation frequency
147 in high-latitude regions (approximately 2–3 times that at the equator), the original dataset is prone to oversampling in these
148 areas, which can introduce bias. To construct a balanced dataset suitable for clustering analysis, this study implemented a
149 homogenization for the sampling. Specifically, the satellite's observation frequency was calculated as a function of latitude,
150 and sample size for each latitude was adjusted using the ratio of its frequency to that at the equator. Subsequently, precipitation
151 systems were randomly selected from each latitude to ensure a consistent scaled sample size, thereby effectively addressing
152 the issue of uneven sampling. Finally, a total of 8,924,307 PSs, as defined in Section 2.2, were obtained for subsequent analysis.

153 2.3. Methods

154 In this study, two distinct machine learning models, namely k-means clustering and principal component analysis (PCA) were
155 used. Both models were trained and evaluated via the Python scikit-learn package. These models are briefly described below.
156 The k-means algorithm is a widely used unsupervised clustering method in machine learning because of its simplicity and

157 ~~computational efficiency~~The k-means algorithm is one of the most popular clustering algorithms among machine learning
158 ~~algorithms. It is one of the most popular unsupervised clustering algorithms due to its efficiency~~ (Jain, 2010). The algorithm
159 follows a three-step process. Initially, it aims to select initial cluster centers by randomly obtaining sample coordinates from
160 the dataset and assigning each sample to its nearest cluster center. Next, it computes the mean of all sample points assigned to
161 each previous cluster center to establish new cluster centers. Finally, the algorithm aims to evaluate the differences between
162 the new and old cluster centers. If differences are present, the last two steps are repeated until the cluster centers stabilize and
163 no longer shift (Jain, 2010).

164

165 PCA is a classical dimensionality reduction tool in machine learning (Gang and Bajwa, 2022). PCA is based on the linear
166 combination of target features to construct the principal subspace, and the variance is then employed to measure the information
167 content with the aim of identifying the linear subspace with the maximum variance (Marukatat, 2023). In summary, PCA aims
168 to transform numerous pertinent features into a comparatively limited number of irrelevant ones, thereby retaining as much of
169 the informational content of the original data as possible (Gang and Bajwa, 2022). Considering that there are 176 vertical
170 layers of GPM DPR products, if all DSD data were used as input parameters, the clustering effect could be poor because of
171 the high dimensionality. In this study, PCA was adopted to reduce the dimensionality of the data while striking a balance
172 between information loss and the optimal number of parameters to be retained (Festa et al., 2023; Jolliffe and Cadima, 2016).

173 Specifically, PCA was independently applied to the vertical profiles of Z_e , D_m , and N_w , each of which originally consists of
174 176 vertical levels. Finally, for each profile of Z_e , D_m , or N_w , the 176 vertical levels are reduced to one single value, which
175 referred to as the first principal component score, capturing the dominant variation in the vertical structure.

176

177 In this study, all the ~9 million PSs derived in section 2.2 are used~~all input parameters were derived from the precipitation~~
178 ~~feature (PF) database, which contains approximately 9 million PFs identified from GPM DPR data. Input parameters of each~~
179 ~~PS variables for k-means clustering were reduced by PCA. They include~~ the maximum precipitation rate near the surface, H_{top} ,
180 the precipitation area, the proportion of stratiform precipitation, the proportion of convective precipitation, the DSD parameters
181 (D_m and N_w)~~and~~ the maximum radar reflectivity parameter (Z_e), and the first principal component score of the vertical profiles
182 of Z_e , D_m , and N_w after dimensionality reduction via PCA.

183 ~~were used as input parameters for the k-means clustering algorithm.~~ These parameters were selected based on their critical role
184 in comprehensively characterizing the features, structure, and microphysical processes of precipitation systems. Among them,
185 the maximum surface precipitation rate and Z_e reflect the intensity of the precipitation process and its echo characteristics,
186 while the precipitation area directly characterizes the spatial differences in both the vertical and horizontal distributions of the
187 system. The H_{top} not only reveals the vertical distribution but also captures the top-level information of the precipitation cloud
188 through the maximum reflectivity height. Introducing the proportions of stratiform and convective precipitation facilitates the
189 differentiation of precipitation types generated by distinct mechanisms, thereby elucidating their evolution patterns and
190 dynamic characteristics. Furthermore, the DSD parameters (D_m and N_w) effectively describe the size distribution of

191 precipitation particles and their intrinsic physical processes, providing an essential basis for an in-depth understanding of
192 precipitation microphysics. Collectively, constructing a multidimensional precipitation feature space with these parameters
193 enhances the accuracy and robustness of the clustering analysis.

194

195 The quality of clustering was evaluated by analyzing different clustering structures derived from the same dataset. Common
196 clustering performance metrics include ~~The most commonly employed performance metrics, such as~~ the sum of squared errors
197 (SSE), Davis Bouldin (DB) index, Calinski-Harabasz (CH) Score (El Khattabi et al., 2024) and silhouette index, which are
198 widely used to evaluate clustering effectiveness and quality can be utilized to assess the effectiveness and quality of clustering
199 algorithms (Ay et al., 2023). In this case, the DB index was calculated by computing the average sum of the intraclass distances
200 between any two clusters divided by the distance between the centers of those two clusters and obtaining the maximum value.

201 The DB index can manage clusters of different sizes and densities with a high degree of robustness to noise and outliers.

202 ~~The DB index is calculated by computing the average sum of intraclass distances between clusters, divided by the distance~~
203 ~~between their respective centers, with the final value determined by the maximum across all clusters.~~ A lower DB index
204 indicates better clustering performance (Sowan et al., 2023). Additionally, the CH score, which assesses clustering
205 compactness and separation, was also considered. Higher CH scores indicates better-defined clusters. Algorithms with
206 clustering numbers ranging from 3 to 20 were executed, and the resulting change in the DB index and CH score was plotted
207 (refer to Fig. S1 in the Supplementary Material). As shown in Figure S1, the DB index reaches its minimum at $K = 8$ and then
208 increases rapidly, whereas the CH score attains its maximum at $K = 11$ with only a slight improvement compared to $K = 8$.
209 Considering the overall trends of both indices, $K = 8$ provides a more balanced and stable clustering structure and was therefore
210 selected as the optimal number of clusters. ~~The results show that when $K = 8$, the DB index reaches its lowest value, while the~~
211 ~~CH score remains relatively high, indicating a well-balanced clustering structure. Therefore, the optimal number of clusters is~~
212 ~~eight.~~

213 ~~Combining all the features of the PSs described in Section 3, the Cluster 1–8 could be regarded as four non-extreme PS (high-~~
214 ~~latitude shallow PS, subtropical shallow PS, moderate PS, deep PS) and four extreme PS (extreme deep PS, strong PS, extreme~~
215 ~~strong PS, and marine extreme PS), which are listed here for the convenience of understanding the following context.~~

216 3. Results and discussion

217 3.1. Global distributions

218 After clustering, each cluster was characterized by its unique precipitation and spatial distribution characteristics, including
219 D_m , MAXHT20/30/40, and convective/stratiform fractions and so on. Table 1 summarizes ~~shows~~ the statistics of various
220 parameters for the eight types of PS, while Figure 1 illustrates their spatial distributions. For clarity in the subsequent discussion,
221 Clusters 1–8 were grouped and named based on their spatial distributions (Fig. 1) and key precipitation characteristics (Table
222 1). Four non-extreme precipitation systems were identified (high-latitude shallow, subtropical shallow, moderate, and deep

223 PS), along with four extreme precipitation systems (extreme deep, strong, extreme strong, and marine extreme PS). Overall,
224 extreme precipitation systems account for a smaller proportion and~~but~~ exhibit higher MAXHT20/30/40, larger D_m , and
225 stronger precipitation rates compared with non-extreme precipitation systems. Geographically, high-latitude shallow
226 precipitation systems are mainly distributed north of 40°N and south of 35°S, subtropical shallow precipitation systems occur
227 primarily within about 20° on both sides of the equator, and marine extreme convection is mostly located over the ocean.

228

229

230 ~~Table 1 shows the statistics of various parameters for the eight types of PS. These~~ numbers in Table 1 include abundant
231 information and verify the rationality of the objectively clustering algorithm. First, the numbers of the various types of PSs
232 differed significantly. The two types of shallow PSs (high-latitude shallow PS and subtropical shallow PS) accounted for 81.44%
233 of the total PS count. The proportions of deep and moderate PSs were 2.41% and 15.50%, respectively. The other four types
234 of PS are regarded as extreme PS (extreme deep PS, strong PS, extreme strong PS, and marine extreme PS) because their ratios
235 of the total PS are less than 1%, accounted for only 0.39%, 0.22%, 0.02%, and 0.01%, respectively. In the non-extreme PS,
236 MAXHT20 is generally positively related to the precipitation rate (Table 1). However, in the extreme PS, the correlation
237 between the extreme precipitation rate and MAXHT20 is not clear. For example, that the mean value of the maximum
238 precipitation rate in marine extreme PS was the highest among the eight types of PSs, although its MAXHT20 was less than
239 that in extreme strong PS and close to that in extreme deep PS. This result is consistent with other studies noting a weak link
240 between the heaviest rainfall and the highest storm top (Hamada et al., 2015). Although the convective intensity of extreme
241 deep PS is not significantly higher than that of deep PS, it exhibits a substantially larger precipitation area and maximum
242 precipitation rate.

243

244 High-latitude shallow PS was most prevalent at midlatitudes and high latitudes, where snowfall and sleet are more frequent
245 than at low latitudes. Notably, high-latitude shallow PS were dominated by stratiform precipitation, with stratiform pixels
246 accounting for 88.63%. Meanwhile, approximately 86.60% of the PS exhibited surface temperatures higher than 0 °C. A study
247 confirmed that at high latitudes and in polar regions, more than 25% of precipitation falls as snow (Lerber et al., 2018). This
248 is consistent with the observations from high-latitude shallow PS. Additionally, an analysis of high-latitude shallow PS by
249 latitude revealed that with increasing latitude, the number of samples generally increased. Moreover, the number of PSs with
250 echo top heights less than 2.5 km increased with latitude. During the winter season at 65°S, PSs with echo top heights below
251 2.5 km accounted for approximately 50% of the total PSs there. This is likely due to the influence of the low surface temperature
252 and weak convection (refer to Fig. S2 in the Supplementary Material).

253

254

255 Subtropical shallow PS primarily occurred over the ocean ~~where is~~ dominated by the subtropical high, with a relatively limited
256 degree of overlap with moderate PS and deep PS (Fig. 1). The mean MAXHT20 value in subtropical shallow PS was only

257 3.29 km, and the proportion of convective precipitation was the highest among all the types of PSs, exceeding 90%. Compared
258 with those of the other PSs, subtropical shallow PS exhibited the smallest precipitation area. Moreover, it was rarely found
259 over land. These results support the conclusion that subtropical shallow PS is associated with isolated shallow convection over
260 the ocean, which has been the topic of interest in previous studies (Chen and Liu, 2016; Chudler et al., 2022; Houze Jr. et al.,
261 2015).

262

263

264 The geographic distribution patterns of deep PS and moderate PS were approximately the same (Fig. 1). The number of
265 occurrences in the maritime continent (MC), Indian Ocean, Atlantic Ocean, Amazon rainforests and Pacific Ocean were
266 relatively high. These regions are generally influenced by the Intertropical Convergence Zone (ITCZ). Nevertheless, the deep
267 PS has higher land percentage. The mean values of the maximum precipitation rates in moderate PS and deep PS were 6.21,
268 35.94 mm h⁻¹, respectively, whereas those of MAXHT20 were 7.03 and 11.89 km, respectively. As a result, the spatial
269 distribution of deep PS is very similar to that of the deep convection core (Ni et al., 2019), which is defined as MAXHT20
270 larger than 10 km.

271

272 Strong PS, extreme deep PS, extreme strong PS, and marine extreme PS demonstrated low sample sizes. However, their
273 precipitation areas are significantly larger than non-extreme PS (Table 1). The location of extreme deep PS is similar with
274 moderate and deep PS, with larger values for most parameters. ~~(2017)(2021)~~In the extreme strong PS, the proportion of land
275 pixels reaches 81%, with significant concentrations in near-equatorial Africa, America, India, the southeastern U.S., and South
276 America. The average maximum precipitation rate in extreme strong PS was 156.37 mm h⁻¹, and MAXHT40 reached 12.32
277 km, which is the highest among all the types of PSs. The high MAXHT40 value indicates strong updraft in the middle
278 troposphere, which is a hallmark of intense convection and favors hail formation (Kumar et al., 2023; Zipser et al.,
279 2006) ~~favorable for hailstone formation~~. Therefore, the spatial distributions of hailstorms in extreme strong PS were very
280 similar to those of ~~hailstorms with large hailstones on the ground (Marra et al., 2017)~~ the global hail map derived from
281 spaceborne precipitation radar (Ni et al., 2017) and passive microwave sensor (Bang and Cecil, 2021). Marine extreme PS was
282 primarily situated in the near-equatorial marine region, with only 943 PSs and 90% is over the ocean. The mean maximum
283 precipitation rate in marine extreme PS was 178.30 mm h⁻¹, ranking first among the eight types of PSs. Although the
284 MAXHT20 value in marine extreme PS reached 12.81 km, the MAXHT40 value in marine extreme PS was approximately
285 half of that in extreme strong PS, indicating low convection activity in the middle and upper levels. This is consistent with the
286 findings of Liu et al. (2007)(2007), who observed that the difference between cloud-top height and MAXHT20 over land is
287 smaller than that over the ocean, indicating that convective intensity is stronger over land than over the ocean.

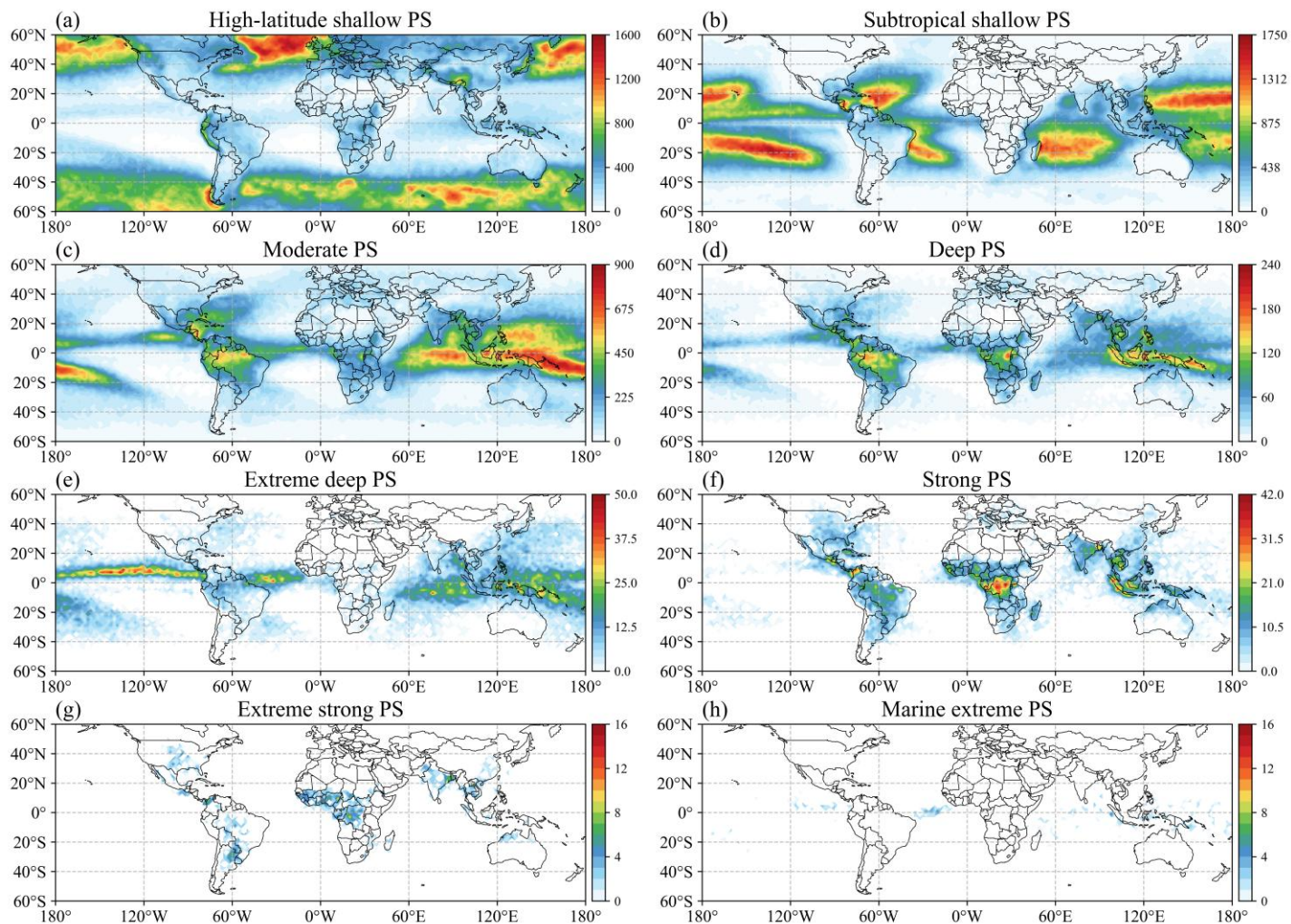
288

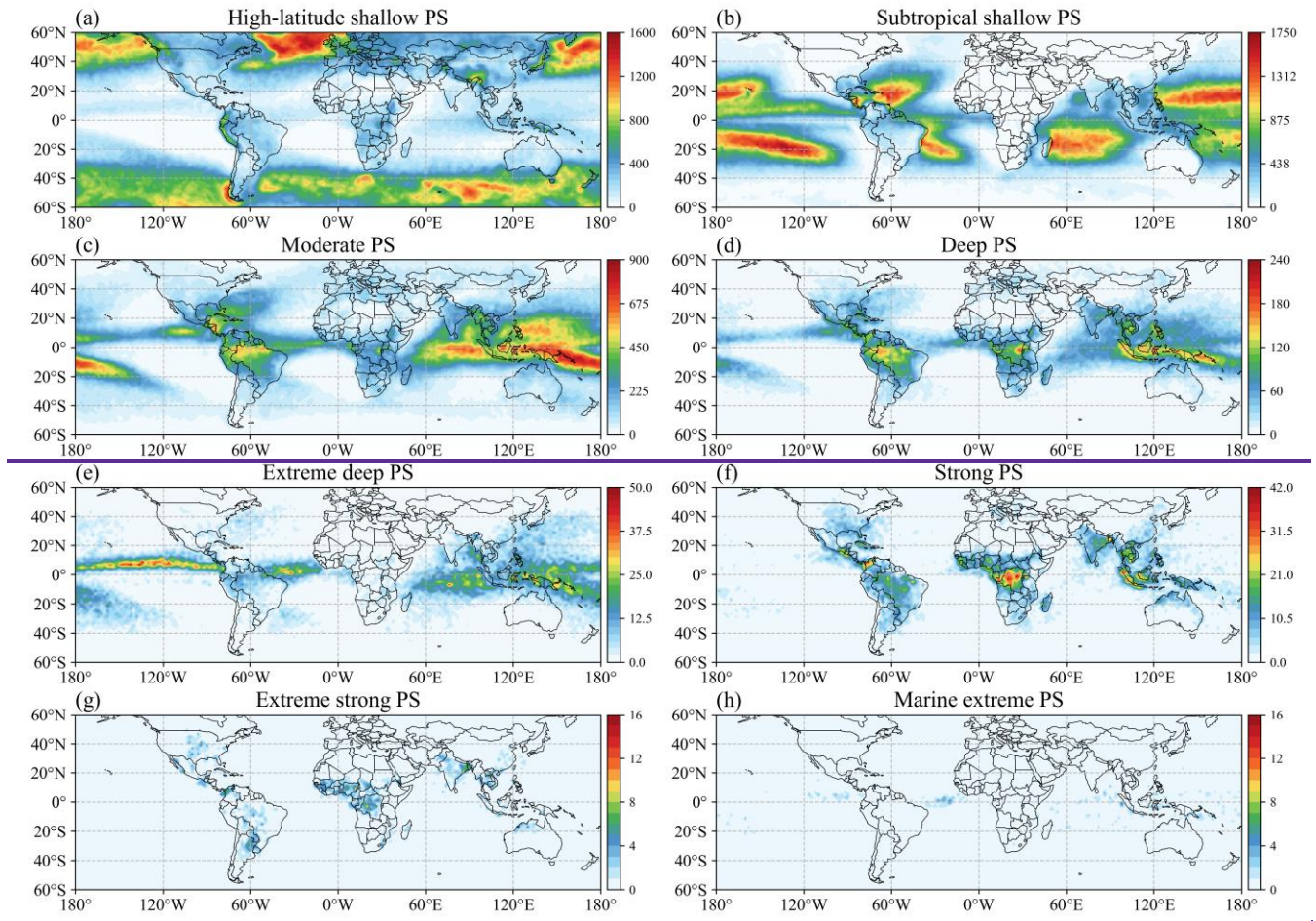
289 Oceanic extreme PS (extreme deep PS and marine extreme PS) with a high fraction of ocean pixels, exhibit have a significantly
290 larger-mean precipitation coverage area exceeding 36000 km², significantly larger than continental extreme PS (strong PS and

291 extreme strong PS). This spatial distribution aligns with previous findings that the most extensive [precipitation systems](#) PS are
292 predominantly located in oceanic regions [according to the study of Zhang and Wang \(Zhang and Wang, 2021\)](#). Furthermore,
293 continental extreme PS display markedly stronger convective intensity. This disparity is largely attributable to the observation
294 that the heaviest PS generally occur over tropical land, the Western Pacific warm pool, the North American Great Plains, and
295 Argentina, whereas the most severe convective storms are predominantly observed over continental areas (Liu and Zipser,
296 2015).

297

298





300

301

Figure 1. Spatial distributions ($2^\circ \times 2^\circ$) of the PS counts from 2018 to 2022

302

303 **Table 1.** Precipitation parameters for the different types of PSs. (* indicate that in high-latitude shallow PS and
304 subtropical shallow PS, approximately 80% of the samples do not reach 40 dBZ. Therefore, the mean MAXHT40 for these
305 samples is recorded as 0.)

	high- latitude shallow PS	subtropical shallow PS	Moderate PS	deep PS	extreme deep PS	strong PS	extreme strong PS	marine extreme PS
Mean MAXHT20 (km)	3.40	3.29	7.03	11.89	12.67	15.39	17.21	12.85
Mean MAXHT30 (km)	2.63	2.67	5.11	8.65	8.52	13.68	16.31	9.18
Mean MAXHT40 (km)	0.00*	0.00*	3.44	5.53	5.71	8.64	12.32	6.04
Stratiform percentages (%)	88.63	9.46	54.38	53.22	69.90	57.42	53.02	66.83
Convective percentages (%)	5.85	89.95	42.83	44.52	28.16	39.91	44.06	31.56
Land percentages (%)	21.61	6.97	27.96	42.31	15.61	65.37	80.98	10.45
Ocean percentages (%)	78.39	93.03	72.04	57.69	84.39	34.63	19.02	89.55
Mean precipitation (mm h ⁻¹)	1.60	2.35	6.21	35.94	156.67	135.46	156.37	178.30
precipitation Standard deviation (mm h ⁻¹)	1.63	1.92	8.89	50.44	98.44	106.95	103.50	98.61
Number of samples	4,184,547	3,083,077	1,383,261	215,611	34,982	19,790	2,096	943
Mean precipitation area (km ²)	610.57	239.23	2761.46	7009.37	37076.93	18485.91	22521.51	36044.11
>273.15 K frequency (%)	86.60	99.16	99.83	99.97	99.97	99.99	99.99	100.00
2.5 km Mean MAX-log10(N _w) [m ⁻³ mm ⁻¹]	3.47	3.70	4.06	4.49	5.20	4.72	4.88	6.07
2.5 km Mean MAX-D _m [mm]	1.03	1.17	2.26	2.82	2.71	3.04	3.11	2.61
2.5 km Mean log10(N _w) [m ⁻³ mm ⁻¹]	3.23	3.45	3.36	3.39	3.83	3.36	3.35	4.45
2.5 km Mean D _m [mm]	0.85	0.89	1.36	1.50	1.30	1.61	1.71	1.32

306 3.2. Global distributions of microphysical features

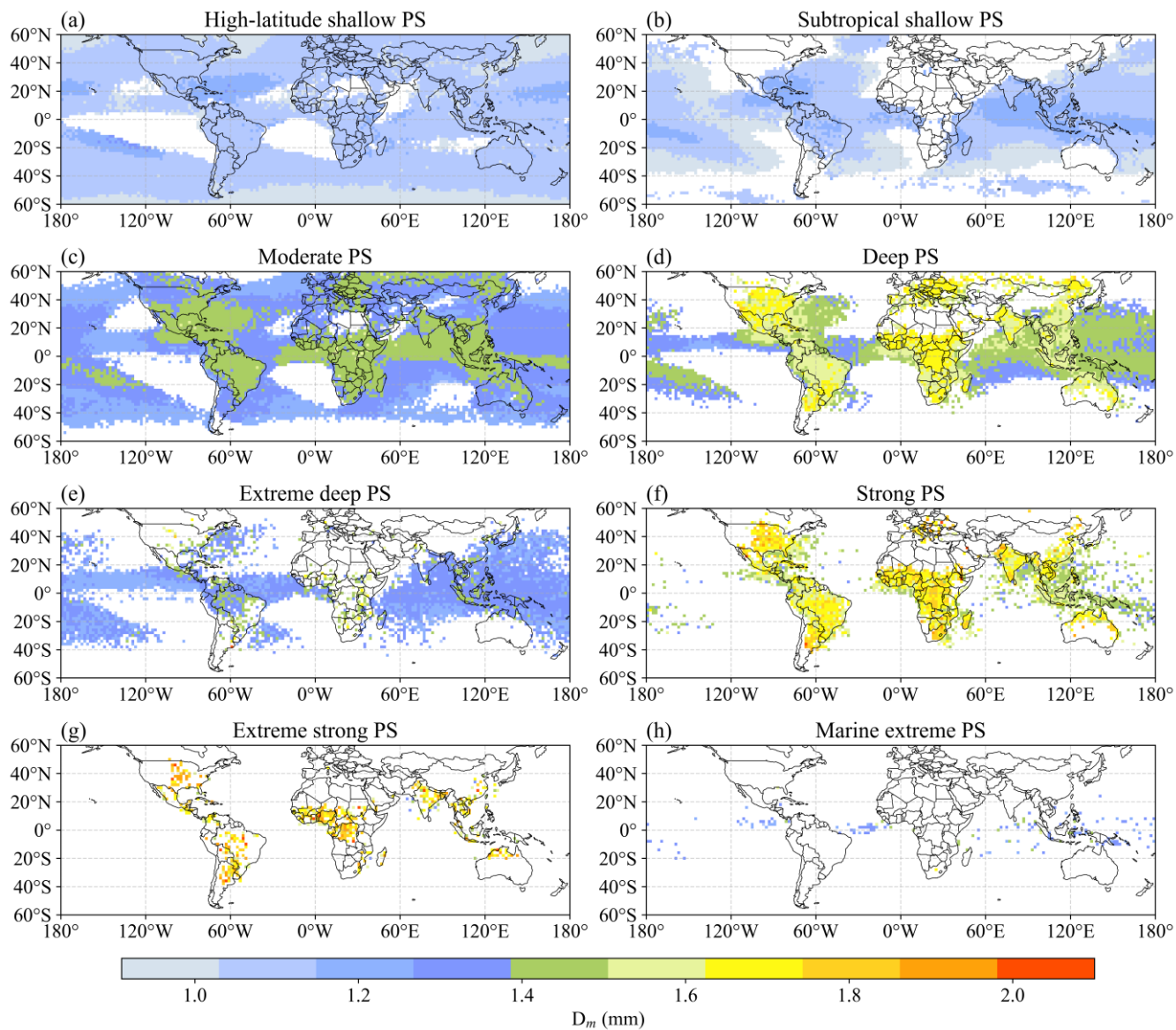
307 Fig. 2 and Fig. 3 show the global distributions of the microphysical parameters for the eight types of PSs. To avoid the influence
308 of ground clutter, in each PS, the mean D_m and N_w values at 2.5 km above the ground surface were analyzed. Notably, there
309 was a significant degree of spatial heterogeneity in each panel. The general conclusion is that continental PSs exhibit a higher

310 D_m than do oceanic PSs. Usually, continental rainfall is associated with high convective activity in which clouds produce large
311 raindrops. ~~Over land, small raindrops are lifted by updrafts, whereas large raindrops are formed from the melting of larger ice~~
312 ~~crystals~~. In contrast, oceanic rainfall is accompanied by the formation of weak updrafts and the development of a low melting
313 layer, which impedes the formation of large raindrops and results in a high concentration of small raindrops (Saha et al., 2022;
314 Seela et al., 2018). Moreover, D_m decreases with increasing latitude, a trend that is especially notable in high-latitude marine
315 regions (refer to Fig. S2c in the Supplementary Material). Cha et al. (Cha and Yum, 2021) noted that snow primarily comprises
316 small particles (~~diameterdiameter~~ < 1 mm). In high-latitude shallow PS, snowfall may become more frequent from the middle
317 to high latitudes, which can result in a decrease in D_m . Notably, the height and thickness of the melting layer may influence
318 raindrop growth (Hu et al., 2024). With increasing latitude, the melting layer becomes thinner, thus reducing the conditions
319 necessary for raindrop growth, which may lead to the formation of a larger number of small raindrops. In the oceanic regions
320 within subtropical shallow PS, the higher sea surface temperature in the tropics is more conducive to convection formation
321 and development. Moreover, D_m varies among the eight clusters in a specific region. For example, in the Amazon region,
322 moderate PS exhibits a lower D_m than deep PS does.

323

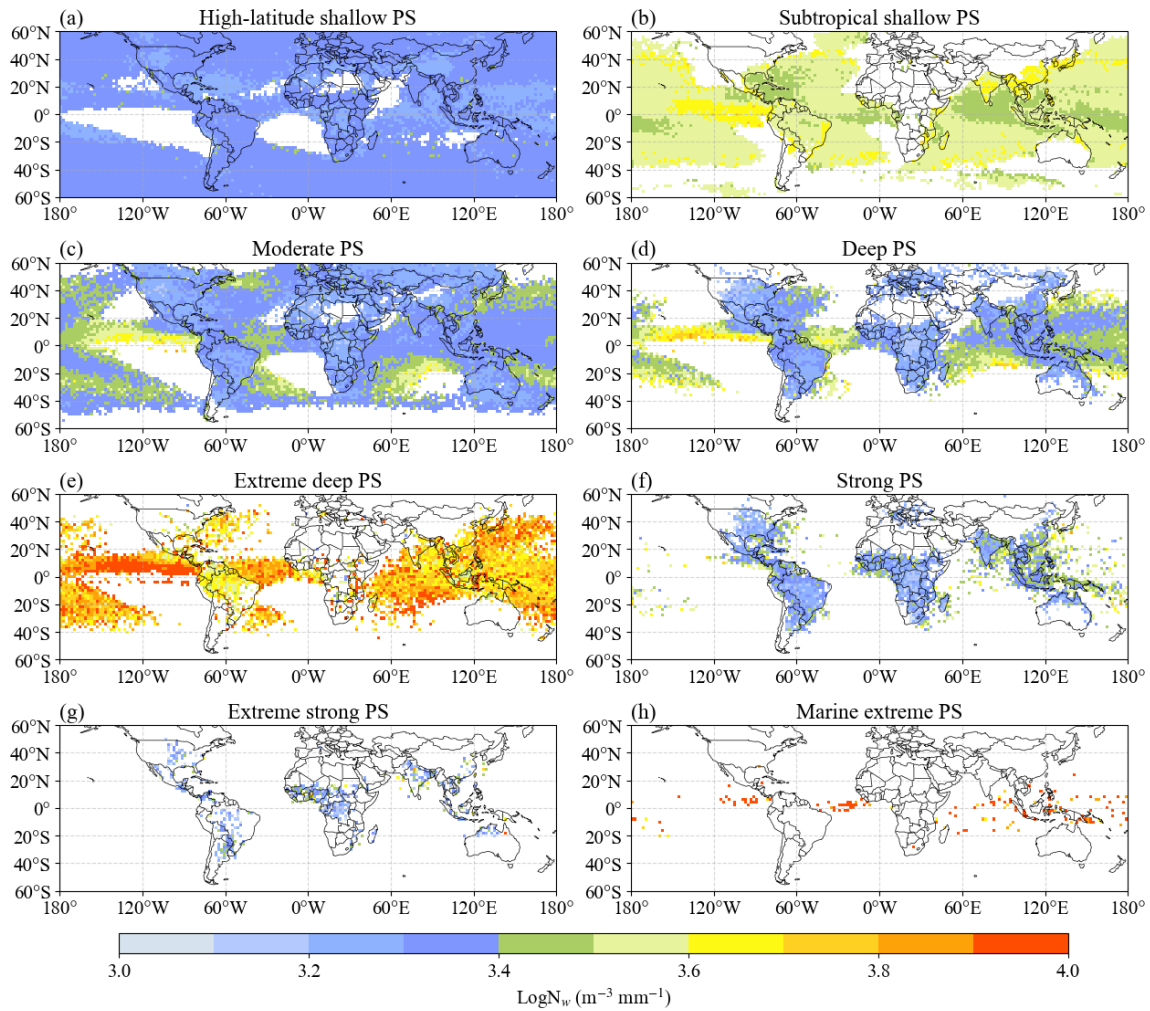
324 Similar to D_m , there is a distinct contrast in N_w between continents and oceans (Das and Chatterjee, 2018). Continental rainfall
325 is usually associated with the cold rain mechanism, whereby raindrops grow as ice particles (Gupta et al., 2023). In contrast,
326 oceanic rainfall is associated with a warm rain regime, in which raindrops grow via a collision-agglomeration mechanism.
327 Consequently, N_w over land is less than that over oceans (Suh et al., 2016). For the same PS, N_w is high in areas with small D_m
328 values and conversely low in areas with large D_m values. For example, in extreme deep PS, the D_m value over the eastern near-
329 equatorial Pacific Ocean, which reaches approximately 1.18 mm, is smaller than that of the other oceanic regions. However,
330 N_w is significantly greater than those in the other regions. In strong PS, the D_m values in near-equatorial Africa and the eastern
331 United States are greater than those in other regions, but the N_w values are lower than those in other regions. It is possible that
332 D_m and N_w may be negatively correlated for the same PS.

333



334

335 **Figure 2.** Spatial distributions of the mass-weighted mean diameter (D_m) for the eight PS clusters at a height of 2.5 km.



336

337 **Figure 3.** Similar to Fig. 2. but for $\text{log}_{10}(N_w)$.

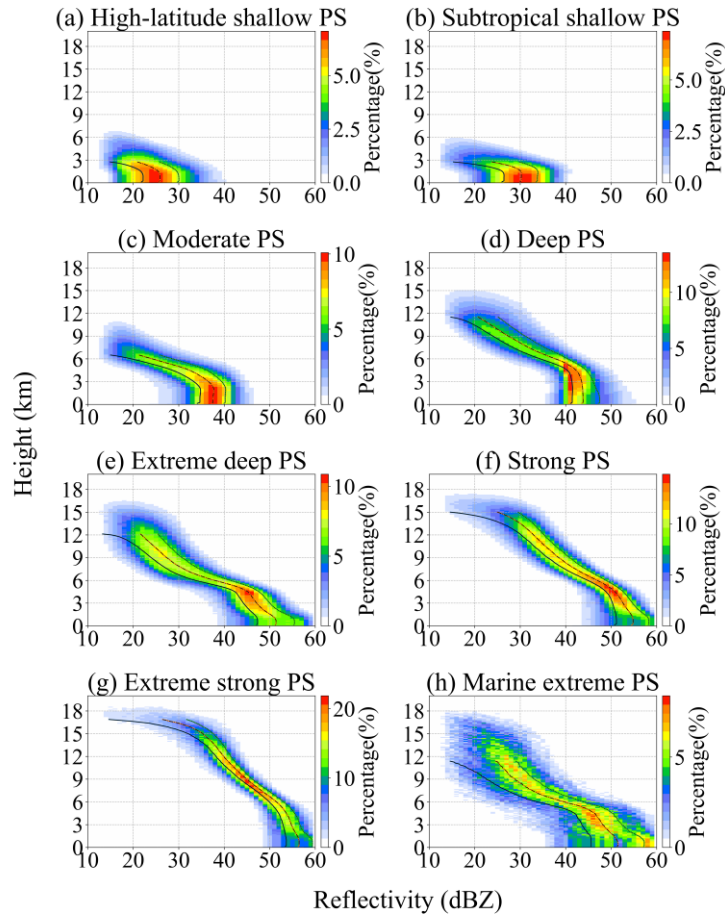
338 3.3. Vertical structure of the different PS types

339 The contoured frequency by altitude diagrams (CFADs) of D_m , N_w , and the maximum radar reflectivity for the eight clusters
 340 are shown in Fig. 4/5/6. Figure 4 shows the CFAD of the maximum radar reflectivity profiles. The results revealed high echo
 341 tops for deep PS, extreme deep PS, strong PS, and extreme strong PS, and low echo tops for high-latitude shallow PS and
 342 subtropical shallow PS. Extreme strong PS attained an echo top height greater than 18 km, and it also exhibited the strongest
 343 convection at the middle level. Its geographic distribution was exclusively terrestrial, which is consistent with other studies
 344 concluding that deep convective cores occur mostly over land (Houze Jr. et al., 2015). Extreme deep PS and marine extreme
 345 PS exhibited sharper decreasing trends from 6–12 km than extreme strong PS, indicating weaker convective updrafts. In
 346 contrast, extreme strong PS had stronger updrafts, producing more supercooled liquid droplets and large ice–water vapor

347 ~~condensates. Extreme deep PS and marine extreme PS exhibited sharper decreasing trends from 6–12 km than that in extreme~~
348 ~~strong PS. Therefore, extreme strong PS encompassed a greater amount of supercooled liquid droplets or large ice–water vapor~~
349 ~~condensates produced by strong convective updrafts than that in extreme deep PS and marine extreme PS (Jiang, 2012). Owing~~
350 ~~to the lack of strong updrafts in extreme deep PS and marine extreme PS, the reflectivity rapidly decreased with height above~~
351 ~~the freezing level. Due to weaker updrafts in extreme deep PS and marine extreme PS, reflectivity decreased rapidly with~~
352 ~~height above the freezing level. In contrast, extreme deep PS and marine extreme PS showed lower 40 dBZ echo tops and a~~
353 ~~more rapid decrease in reflectivity above the freezing level. This suggests relatively weaker mid- and upper-level updrafts,~~
354 ~~which limit the vertical transport of ice particles and reduce the abundance of supercooled liquid and large condensate. In~~
355 ~~addition, in four extreme PSs, reflectivity exceeding 50 dBZ below the freezing layer and remaining above 40 dBZ above the~~
356 ~~melting layer is a characteristic signature of hail profiles, further confirming the presence of hail within strong convection~~
357 ~~(Bang and Cecil, 2021).~~

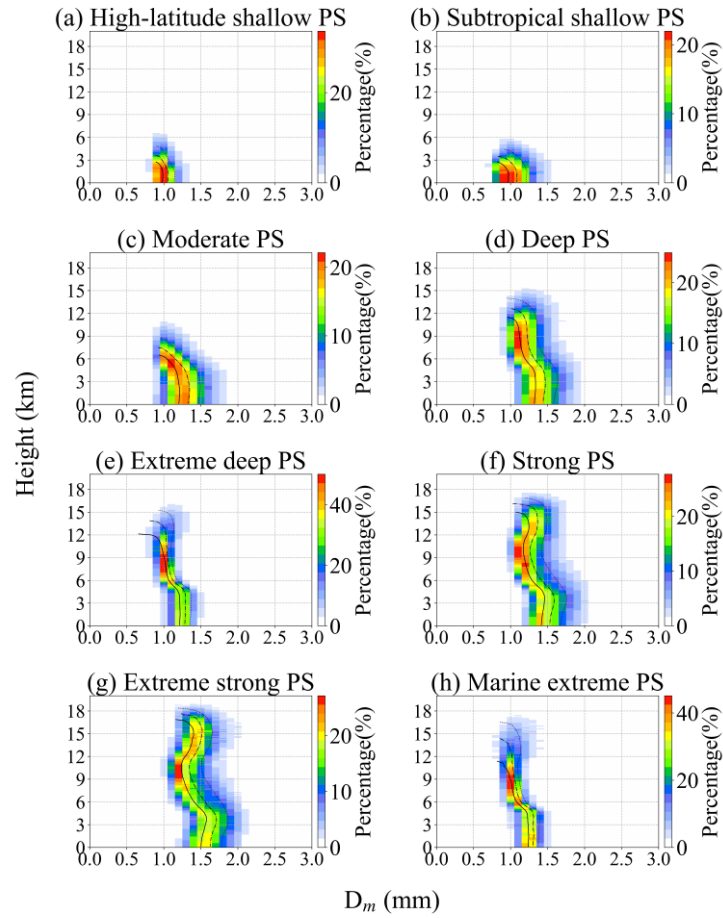
358

359 Table 1 indicates that the land proportion of extreme strong PS was much greater than that of extreme deep PS and marine
360 extreme PS. Additionally, land indicates a dry adiabatic lapse rate, which results in greater buoyancy and allows for stronger
361 updrafts to lift ice crystals higher into the atmosphere. As a result, the maximum radar reflectivity in the middle levels at high
362 altitudes decreased more slowly in extreme strong PS. High-latitude shallow PS and subtropical shallow PS yielded low echo
363 tops of less than 6 km, indicating low convective intensity. Therefore, subtropical shallow PS could be identified as being
364 associated with isolated shallow convection over the ocean, especially the region dominated by the subtropical high. ~~(Bang~~
365 ~~and Cecil, 2021)~~



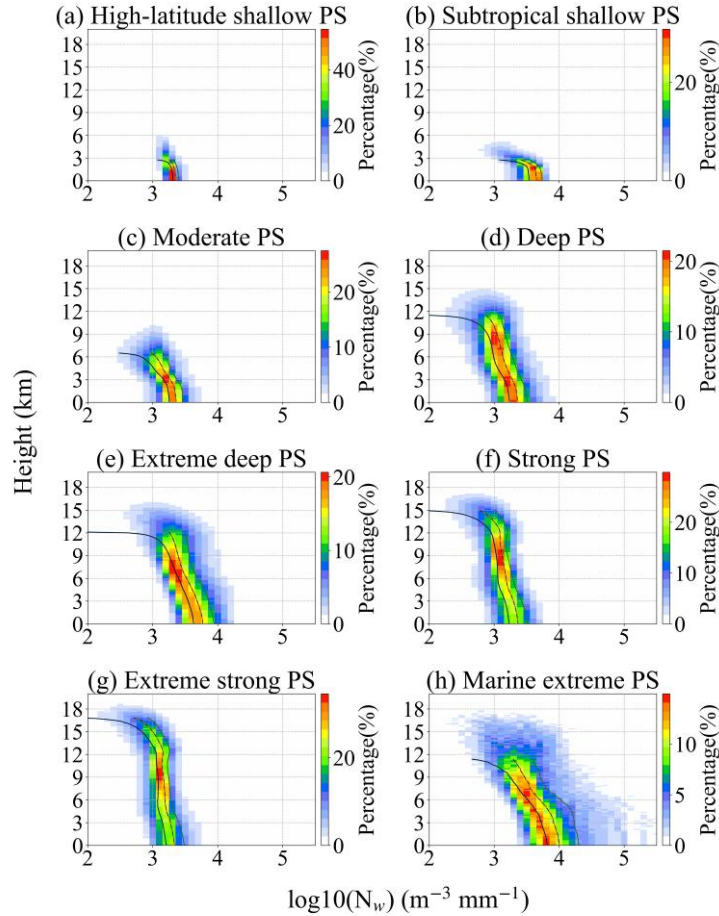
366

367 **Figure 4.** Contoured frequency by altitude diagrams (CFADs) of the maximum radar reflectivity for the eight distinct PS
 368 clusters. The solid lines indicate the 25th percentiles; the dashed-dotted lines indicate the 50th percentiles; the dotted lines
 369 indicate the 75th percentiles.



370

371 **Figure. 5.** Similar to Fig. 4, but for D_m .



372

373 **Figure. 6.** Similar to Fig. 4, but for $\log_{10}(N_w)$.

374 Figure 5 shows the CFAD of D_m for the eight types of PSs. Generally, deep convections (deep PS, extreme deep PS, strong
 375 PS, extreme strong PS, and marine extreme PS) produce different D_m values in the regions above and below approximately 5
 376 km. Moreover, strong PS and extreme strong PS exhibited wider distributions than those of extreme deep PS and marine
 377 extreme PS. For deep PS, strong PS, and extreme strong PS, D_m below 4.8 km did not change much or slightly increased along
 378 with height, but the value decreased between 4.8 and 6.9 km. In extreme strong PS, the vertical structure of D_m was more
 379 complex. Extreme strong PS exhibited three regimes according to the variations in D_m . The first regime was observed between
 380 0 and 4.1 km, where D_m increases with altitude. This is consistent with other papers involving the use of ground-based radar
 381 observations and reporting that D_m of deep convective precipitation decreases with decreasing height near the surface (Marzuki
 382 et al., 2023). The observed decrease in D_m may be related to the continued breakdown of large isolated raindrops in the

383 atmosphere. The second regime was observed above the freezing level, from 4.1 to 10 km, where D_m decreases with altitude.
384 In this regime, the updraft in deep convection was decreased (Uma and Rao, 2009). The decline in updraft decreased the size
385 of the particles that can be retained in the cloud. The rapid changes of D_m between the two regimes might be due to the changes
386 of precipitation phase across the melting layer. As revealed by Mroz et al. (Mroz et al., 2024), the routinely retrieval algorithm
387 results in rapid changes of D_m and mass flux around the melting level, because the DPR observations cannot quantify ice
388 particle content and their size above the stratiform rain regions. Finally, the third regime was observed between 10 and 18 km,
389 where D_m increases with altitude and where strengthened updrafts are often observed (Becker and Hohenegger, 2021).
390 Although both high-latitude shallow PS and subtropical shallow PS were shallow PSs, subtropical shallow PS had a wider
391 distribution of D_m than high-latitude shallow PS. One possible reason is that in shallow oceanic convection, the breaking of
392 large raindrops broadens the DSD.

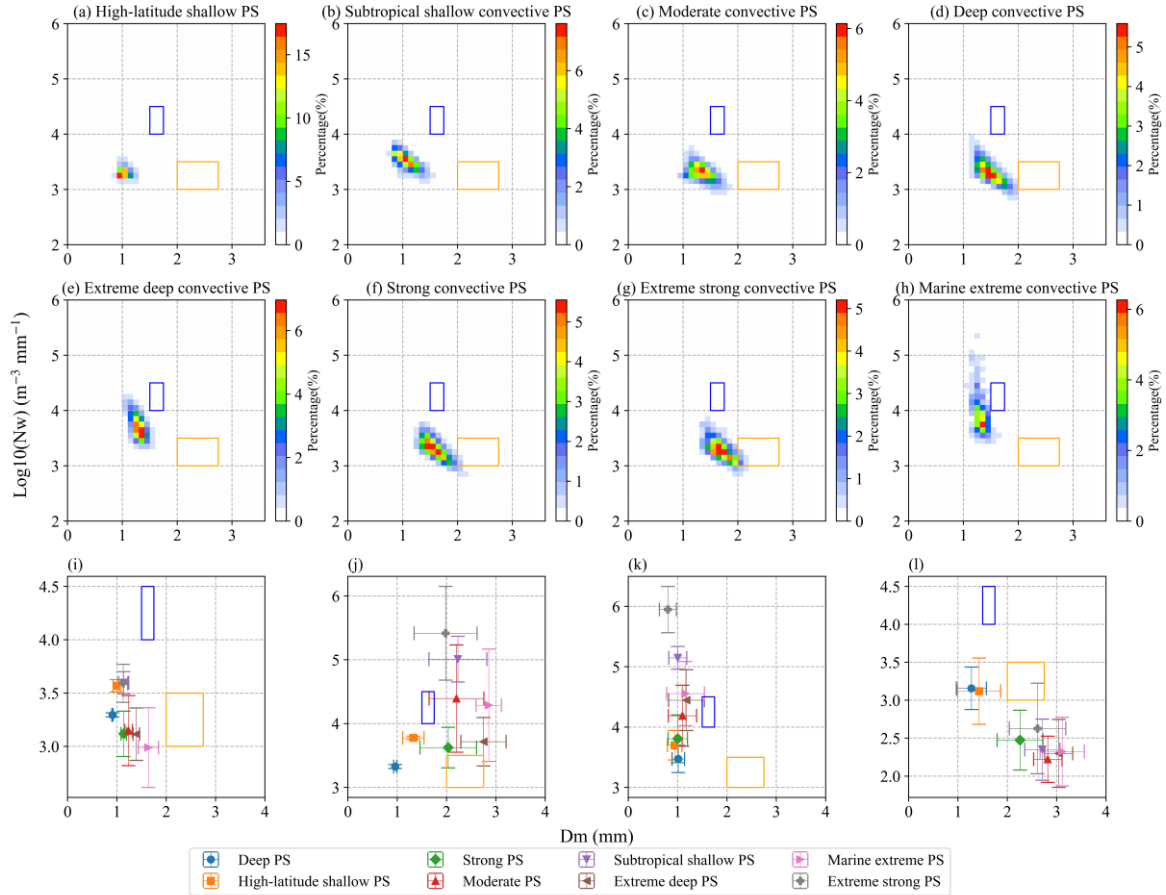
393

394 Figure 6 shows the CFAD of $\log_{10}(N_w)$ for the different types of PSs. In general, N_w decreases with increasing altitude. The
395 distribution range of N_w for shallow PSs was relatively small. Moreover, the N_w distribution range of subtropical shallow PS
396 was larger than that of high-latitude shallow PS. Among PSs with intense convection, PSs with a greater proportion of land
397 coverage exhibited more concentrated N_w values, whereas PSs with a greater proportion of ocean coverage exhibited higher
398 N_w values. For example, the N_w values of strong PS and extreme strong PS were smaller and narrower than those of ocean-
399 dominated deep PS, extreme deep PS and marine extreme PS. This finding is consistent with the conclusions of other studies
400 (Kumar et al., 2024). One possible explanation is that the slower updrafts over ocean regions result in higher concentrations
401 of smaller condensates at lower altitudes. Moreover, for both D_m and N_w , the four non-extreme convective PSs exhibit little
402 vertical variation below the melting layer, which may be attributed to a balance between coalescence and breakup processes.

403 3.4. DSD characteristics at a height of 2.5 km

404 Figure 7a-h show the frequency distributions of the mean D_m and $\log_{10}(N_w)$ values observed at 2.5 km above ground level.
405 The mean D_m values for the eight types of PSs were 0.85, 0.89, 1.36, 1.50, 1.30, 1.61, 1.71, and 1.32 mm, and the corresponding
406 $\log_{10}(N_w)$ values for the eight types of PSs were 3.23, 3.45, 3.36, 3.39, 3.83, 3.36, 3.35, and 4.45 $m^{-3} mm^{-1}$, respectively are,
407 as detailed in Table 1. Generally, all the distributions shown in Fig. 7a-h greatly deviate from the parameters of continental
408 convection and maritime convection defined by Bringi et al. (Bringi et al., 2003). One reason is that the mean values of D_m
409 and N_w for one PS were considered here, whereas Bringi et al. (Bringi et al., 2003) separated the observation samples into
410 stratiform and convection samples. Moreover, the DSDs observed by disdrometers are generally cumulative observations of a
411 single storm at one fixed location and differ from the results for each PS in this study, which represent the instantaneous
412 occurrence of a storm. With the most intense convection at the middle level, extreme strong PS was the closest to continental
413 convection (Fig. 7d), whereas marine extreme PS was the closest to maritime convection (Fig. 7e). For most PSs, D_m and N_w
414 were negatively correlated, with greater dispersion of D_m than that of N_w . However, it should be noted that the observed
415 correlations between D_m and N_w may partly reflect be due to the retrieval assumptions in the GPM algorithm, which enforces

416 a correlation between D_m and precipitation rate (Chase et al., 2020), rather than purely physical relationships. Moreover, the
 417 shallow PSs, such as high latitude shallow PS, exhibited lower D_m and N_w values and more concentrated distributions than
 418 those of the deep PSs, such as those in deep PS.



419

420 **Figure 7.** (a-h) Two-dimensional frequency distributions of D_m and $\log_{10}(N_w)$ at a height of 2.5 km, and (i-l) statistical values
 421 of $\log_{10}(N_w)$ and D_m for each PS (the bar indicates one standard deviation). (i) Mean values of D_m and $\log_{10}(N_w)$, (j) MAX-
 422 D_m and MAX- $\log_{10}(N_w)$, (k) MAX- $\log_{10}(N_w)$ and D_m at its corresponding position, and (l) MAX- D_m and $\log_{10}(N_w)$ at its
 423 corresponding position for each PS. (the blue and orange rectangles denote the maritime and continental convective clusters,
 424 respectively, in D_m and $\log_{10}(N_w)$ space from Bringi et al. (Bringi et al., 2003)).

425

426 To further compare the mean D_m and N_w values of the different clusters, Figure 7i shows a summary of the mean D_m and N_w
 427 values, with the standard deviation for each type of PS. Marine extreme PS showed a significant abnormal value of N_w , whereas
 428 the N_w value of extreme deep PS slightly deviated from those of the other PS. If only the three extreme deep PSs with the

429 ~~highest echo tops (strong, extreme strong, and marine extreme PS) are considered, D_m and N_w show an inverse~~
430 ~~relationship. However, if only three extremely deep PSs with the highest echo tops, as detailed in Table 1 (strong PS, extreme~~
431 ~~strong PS, and marine extreme PS), were considered, it could be concluded that the larger the D_m value is, the smaller the N_w~~
432 ~~value. Moreover, the other PSs exhibited very similar N_w values.~~ These results might suggest that in deep convection, the DSD
433 parameters at the near-surface level are related to convection intensity parameters. Ni et al. (Ni et al., 2019) revealed that the
434 dual-frequency ratio between the Ku and Ka bands at 12 km was positively correlated with intensity parameters such as
435 MAXHT20/30, partly because stronger updrafts could hold larger ice particles in clouds. ~~However, in shallow convection~~
436 ~~systems such as those in high latitude shallow PS and subtropical shallow PS, the relationship did not hold, which rendered~~
437 ~~the relationship between microphysical parameters and convection parameters complex.~~

438

439 Note that although the mean D_m and N_w values ~~represent the overall features of DSDs in one PS, they~~ do not capture the variety
440 of DSDs in each PS. For example, the DSD might differ between convective and stratiform regions, where the N_w - D_m
441 relationships might vary. To comprehensively demonstrate the microphysical features of PSs, Figure 7j shows the mean MAX-
442 D_m and MAX- N_w values of each PS at 2.5 km ~~above ground level. For extreme PS, MAX- D_m and MAX- N_w were negatively~~
443 ~~correlated, while a positive correlation was observed for non-extreme PS. For extreme PS (extreme deep PS, strong PS, extreme~~
444 ~~strong PS, and marine extreme PS), a negative correlation was found between MAX D_m and MAX N_w , similar to the mean~~
445 ~~D_m and N_w values shown in Fig. 7h. However, for the non-extreme PS, MAX D_m and MAX N_w exhibited positive correlations.~~
446 A similar relationship is also shown in Fig. 7k, which suggests a relationship between MAX- N_w and the corresponding D_m
447 value in the MAX- N_w pixels of each PS. Nevertheless, as shown in Fig. 7k, the D_m values of all eight types of PSs were very
448 close. Nevertheless, it could be also found that in the non-extreme PS the D_m increases with MAX- N_w , while in the extreme
449 PS, the D_m decreases with MAX- N_w . Figure 7l shows the relationship between MAX- D_m and the corresponding N_w value in
450 the MAX- D_m pixels of each PS. Interestingly, for all eight types of PSs, MAX- D_m and N_w showed significantly negative
451 correlations. Note that MAX- D_m and MAX- N_w in Fig. 7j are the maximum values for one PS and usually do not occur in the
452 same pixel. Figure 7k-l show the N_w - D_m relationship observed at the same location. Overall, the conclusions generally
453 indicated that deep PSs yield larger MAX- N_w or MAX- D_m values than shallow convection PSs do. Overall, extreme PS
454 exhibited negative correlations between N_w and D_m , whereas non-extreme PS demonstrated positive correlations.

455

456 Ryu et al. (Ryu et al., 2021) analyzed DSDs during three types of heavy rainfall events with different rain intensities. They
457 also reported that D_m increases with increasing rainfall intensity, whereas N_w decreases with increasing rainfall intensity. In
458 this study, we saw a positive relationship between the increase in D_m and MAXHT20 in extreme PS. However, extreme strong
459 PS attained the highest MAXHT20 value, but its precipitation rate was lower than that of extreme deep PS and marine extreme
460 PS. These results suggest a complex relationship between the microphysical parameters and convection features, especially in
461 deep and intense convection systems. Notably, in extreme convection, with strong convection at the top of the storm,
462 attenuation becomes notable at low storm levels, which might influence the retrieval of microphysical parameters. To assess

463 the impact of attenuation on the D_m - N_w relationship, ground-based observations of microphysical properties from disdrometers
464 are needed. Finally, we considered the PS as a whole ~~and did not account for the variations in the D_m and N_w values of each~~
465 ~~PS~~. The microphysical characteristics varied among different pixels. The mean or maximum values of D_m and N_w only reflect
466 part of the total process. Therefore, analyses on the basis of pixel-level observations would improve this work.

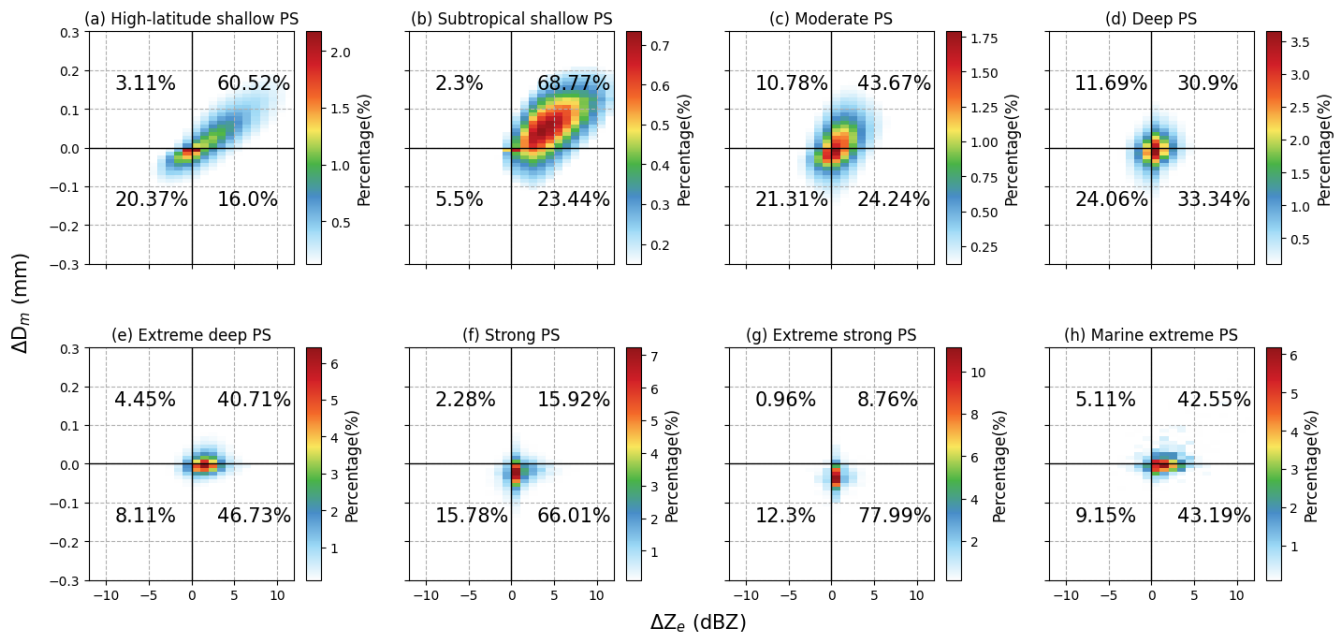
467

468 To gain further insight into the primary microphysical processes associated with the various PS, we employed an investigative
469 approach analogous to that utilized by Kumjian and Prat (~~Kumjian and Prat, 2014~~). To prevent the influence of ground-based
470 clutter, ΔZ_e and ΔD_m values were calculated as the difference between Z_e and D_m at 2 and 3 km above the ground. Specifically,
471 $\Delta Z_e = Z_e^{2\text{km}} - Z_e^{3\text{km}}$ and $\Delta D_m = D_m^{2\text{km}} - D_m^{3\text{km}}$ are calculated. Fig. 8 shows the frequency pattern of ΔZ_e versus ΔD_m for the eight
472 types of PSs. An increase (decrease) in Z_e and D_m indicates that coalescence (breakup) processes dominate. Balanced breakup
473 and coalescence processes result in an increase in Z_e but a decrease in D_m . In contrast, a decrease in Z_e and an increase in D_m
474 are due to predominate evaporation or size sorting processes (Wen et al., 2023).

475

476 The microphysical processes of the different types of PSs were significantly distinct. Notably, the microphysical processes
477 were dominated by coalescence in the two types of shallow PS (Fig. 8a-b). Previous studies have demonstrated that high-
478 latitude shallow PS are more likely to experience the condensation of rain droplets into snow due to the low temperatures in
479 these regions (Thompson et al., 2015). Meanwhile, the coalescence process plays an important role in tropical oceanic shallow
480 convective precipitation (subtropical shallow PS) as demonstrated by Li et al. (~~Li et al., 2024~~). Balanced breakup and
481 coalescence processes in the microphysical processes of extreme PS accounted for more than 40% of the total microphysical
482 processes, significantly exceeding other three types of microphysical processes. The microphysical processes may reach an
483 equilibrium state under high rainfall rates, in which the coalescence and breakup of raindrops are nearly balanced. These results
484 are consistent with Shi et al. (2025), who found that extreme rainfall is primarily driven by vigorous mixed-phase processes
485 and a balance between coalescence and breakup in liquid-phase processes. Extreme deep PS and marine extreme PS
486 encompassed a higher percentage of coalescence processes than strong PS and extreme strong PS did, whereas strong PS and
487 extreme strong PS encompassed a higher percentage of breakup processes.

488



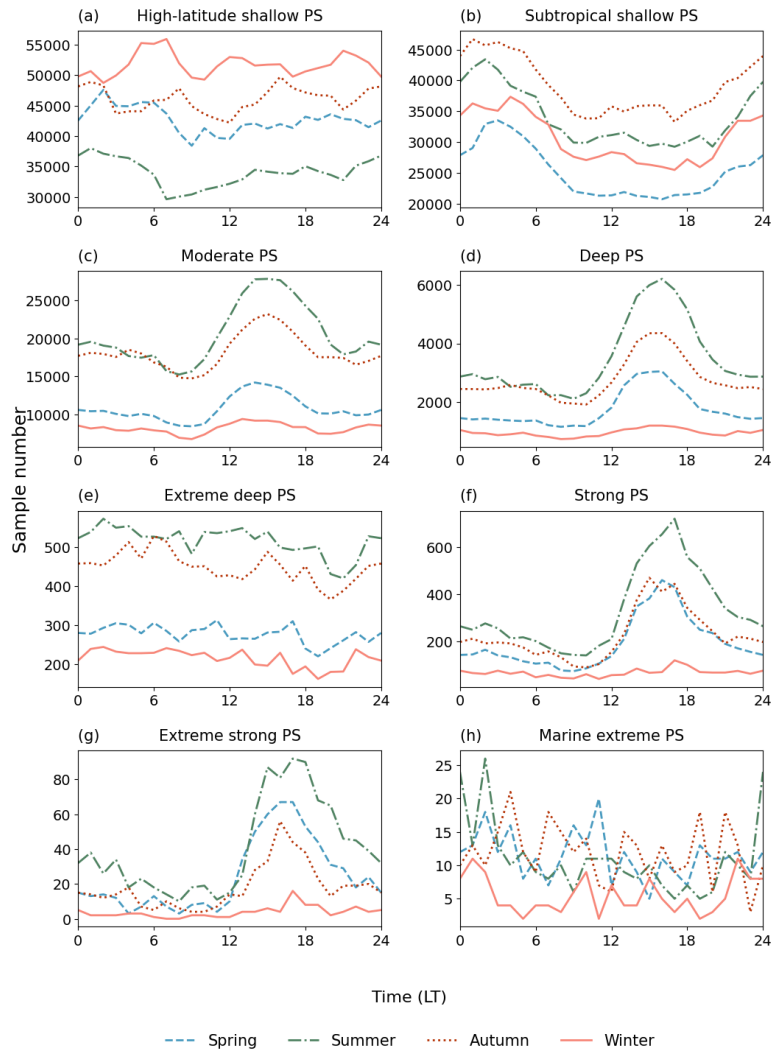
489

490 **Figure 8.** Frequency pattern of ΔZ_e versus ΔD_m between 2 and 3 km for the eight PS clusters.

491 3.5. Seasonal and diurnal cycles

492 In this study, seasons were categorized by fixed calendar months. The Northern Hemisphere seasons were defined as spring
 493 (March–May), summer (June–August), autumn (September–November), and winter (December–February). Conversely, the
 494 Southern Hemisphere seasons followed the opposite pattern: spring (September–November), summer (December–February),
 495 autumn (March–May), and winter (June–August). Based on this classification, the subsequent analysis examines seasonal and
 496 diurnal variations in PS frequency and microphysical parameters. Figure 9 shows the cycles of PS occurrence. Overall, the
 497 seasonal and diurnal cycles differed among the eight types of PSs. Moderate PS, deep PS, strong PS, and extreme strong PS
 498 exhibited cycles like those of continental convection systems, with peaks in the afternoon and in summer. Dominated by
 499 tropical shallow convection over the ocean (Fig. 1), subtropical shallow PS occurred mostly between 0 and 5 a.m. and was
 500 more frequent during the autumn season than during the other seasons, with the lowest occurrence during the spring season.
 501 The other types of PS (high-latitude shallow PS, extreme deep PS, and marine extreme PS) did not show obvious diurnal
 502 cycles, except that high-latitude shallow PS indicated a low peak at approximately 6 am in winter and a valley before noon in
 503 summer. High-latitude shallow PS occurred infrequently in winter. Extreme deep PS occurred more frequently in summer and
 504 autumn, with fewer occurrences in winter. Note that marine extreme PS did not demonstrate obvious seasonal discrepancies,
 505 but shown a peak at night in the summer. Specifically, strong PS and extreme strong PS with a higher proportion over land
 506 exhibit a peak occurrence around 3 p.m. in the afternoon. In contrast, while extreme deep PS and marine extreme PS mostly
 507 over the ocean, show no distinct peak, with frequencies distributed evenly throughout the day with a higher proportion over the

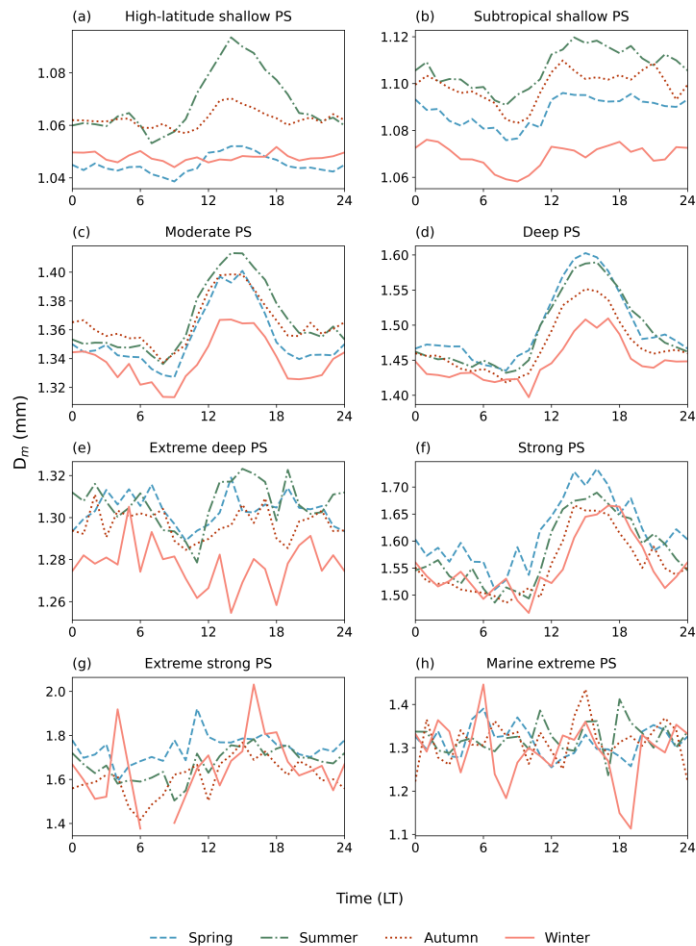
508 ocean shows no distinct peak, with its frequency distributed relatively evenly throughout the day. This difference reflects the
 509 land-ocean contrast in extreme PS, which is consistent with findings from other related studies (Wang and Tang, 2020).
 510



511
 512 **Figure 9.** Diurnal variations in the sample sizes of the eight distinct PS clusters across the four seasons.

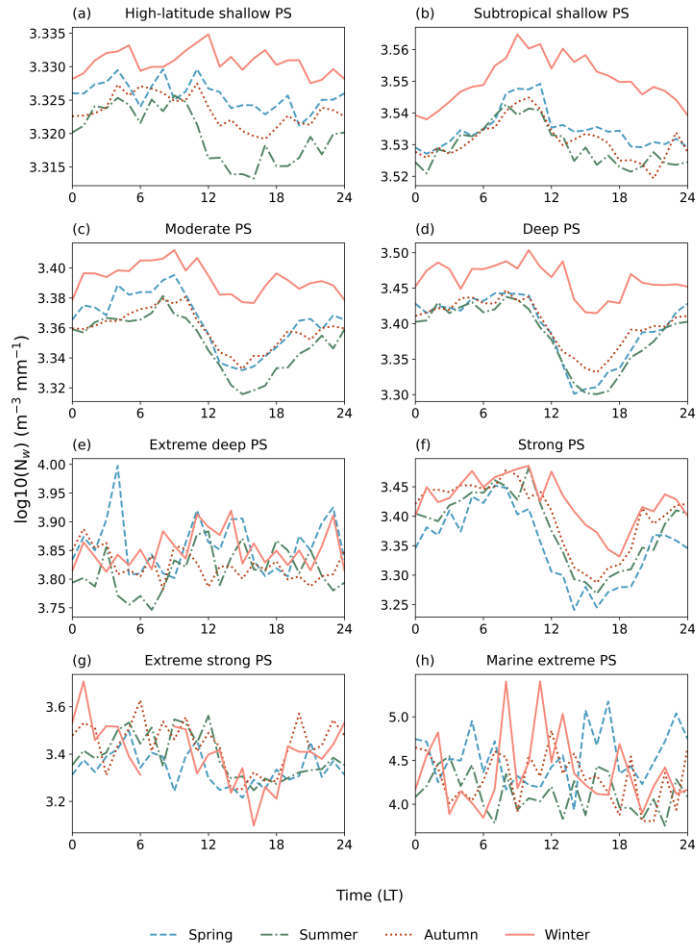
513 Figures 10 and 11 show the seasonal and diurnal cycles of D_m and N_w , respectively. The diurnal cycles of D_m were similar
 514 with those of PS occurrence to some extent. For example, in moderate PS, deep PS and strong PS, both the occurrence and D_m
 515 have peaks in the around 15 pm. One connection between these two parameters is that environments that favor storm
 516 occurrence could also facilitate the development of stronger updrafts, which could promote the formation of large particles in
 517 clouds. Nevertheless, discrepancies are obvious between the cycles of occurrence and D_m . For example, the D_m in the extreme
 518 strong PS did not show obvious diurnal variations. The high-latitude shallow PS shows a peak in the summer (Fig. 10a), which

519 is not found in the diurnal cycle of occurrence (Fig. 9a). In subtropical shallow PS, the diurnal cycle of D_m (Fig. 10b) was the
 520 opposite to that of PS occurrence (Fig. 9b). The diurnal cycles of N_w were basically different with those of D_m and occurrence.
 521 In subtropical shallow PS, moderate PS, deep PS, and strong PS, the N_w peaked in the morning. Nevertheless, the diurnal
 522 cycles of subtropical shallow PS, moderate PS, and deep PS also differed. For example, N_w of subtropical shallow PS at night
 523 was low, whereas N_w of shallow convective PS and moderate PS at night was very close to its peak. Extreme deep PS and
 524 marine extreme PS did not exhibit obvious diurnal cycles of N_w . The extreme strong PS shown low values of N_w in the
 525 afternoon and little variations at night. For high-latitude shallow PS, diurnal variation is not clear except in the summer when
 526 the N_w in the afternoon is the lowest.



527

528 **Figure 10.** Similar to Fig. 9 but for mean D_m value.



529

530 **Figure 11.** Similar to Fig. 9 but for the mean $\log_{10}(N_w)$ value.

531 Similar to the diurnal cycles, the annual cycles of D_m and N_w were opposite in subtropical shallow PS, moderate PS, and deep
 532 PS, of which D_m was the lowest and N_w was the largest in winter. Nevertheless, there were also differences in the annual cycles
 533 of the three types of PSs. For example, in subtropical shallow PS, D_m was the largest in summer, followed by autumn and
 534 spring, whereas the N_w values during the three seasons were very close. Among the extreme PS, N_w and D_m did not exhibit
 535 obvious annual cycles. For high-latitude shallow PS, the highest D_m value occurs in summer and the D_m in winter and spring
 536 were comparable. However, the annual cycle of N_w attained the largest value in winter and the lowest value in summer.

537 4. Conclusions

538 In this study, GPM DPR data were used to objectively classify global PS and analyze the microphysical characteristics of the
539 different types of PS. The main conclusions are as follows:

540

541 1). By conducting an objective classification of global PSs via key parameters such as the convective intensity, radar
542 reflectivity, and DSD parameters, eight distinct types of PSs were identified. These systems were classified on the basis of
543 their unique microphysical and convection properties, providing a detailed understanding of the different precipitation
544 processes worldwide. The eight types of PSs identified are as four types of regular/non-extreme PS (high-latitude shallow PS,
545 subtropical shallow PS, moderate PS, deep PS) and four types of extreme PS (extreme deep PS, strong PS, extreme strong PS,
546 marine extreme PS).

547

548 2). MAXHT20 is generally correlated with the precipitation rate, but this relationship is not clear for extreme PS. The
549 relationship between MAXHT20 and D_m does not follow a simple linear pattern. For extreme PS, MAXHT20 is positively
550 related to D_m at 2.5 km above the ground surface. This may reflect the relationship between higher cloud tops and greater
551 liquid water contents in strongly convective PSs. However, for non-extreme PS, the relationship between MAXHT20 and D_m
552 is more complex and may be influenced by variations in the physical processes of the different PS.

553

554 3). For the same type of PS, D_m over land is greater than that over the ocean. Additionally, D_m exhibits latitudinal variability,
555 particularly in high-latitude shallow PS, where D_m decreases with increasing latitude. Additionally, continental rainfall is
556 associated with lower N_w values due to the cold rain mechanism, whereas oceanic rainfall is associated with higher N_w values
557 resulting from a warm rain regime. Shallow PS generally exhibit narrow distributions of both D_m and N_w , particularly in high-
558 latitude shallow PS. Among the strong PS, PS with a higher land proportion exhibit more concentrated N_w values, whereas
559 those with a greater ocean proportion exhibit larger N_w values. However, the distribution of D_m is the opposite: PS with a
560 higher ocean proportion exhibit more concentrated D_m values than land-dominated PSs do.

561

562 4). The different PS exhibit distinct microphysical processes. In shallow convective PS, such as subtropical shallow PS and
563 high-latitude shallow PS, coalescence processes largely shape the microphysical characteristics, indicating the aggregation of
564 small raindrops in these PS. In contrast, extreme PSs are characterized by balanced breakup and coalescence processes,
565 highlighting a more complex interaction between raindrop formation and breakup. These results emphasize the varying
566 mechanisms that govern microphysical behavior across the different types of PSs. PS types with high precipitation rates are
567 dominated primarily by balanced breakup and coalescence processes, whereas shallow PSs are characterized mainly by
568 coalescence.

569

570 5). The seasonal and diurnal cycles of PSs and their microphysical parameters vary ~~significantly across clusters, with distinct~~
571 ~~patterns observed in different clusters: clusters dominated by e~~Continental convection ~~Cluster indicate~~ peaks in the afternoon
572 and summer, whereas tropical and high-latitude systems exhibit unique seasonal and diurnal cycles, often with opposite trends
573 between D_m and N_w .

574

575 Classifying PS is essential for increasing the understanding of the microphysical processes that govern cloud development and
576 precipitation formation across various climatic regimes. This classification enables the identification of specific mechanisms
577 that influence rainfall characteristics, such as droplet formation, growth, and distribution, which are vital for accurate weather
578 predictions and climate modeling. This study revealed the global distribution characteristics of different types of PS and
579 elucidated the variations in microphysical properties across regions with distinct climatic and geographic conditions.

580

581 In this study, each PS was treated as integrated entity, without considering the variations in D_m and N_w within each system.
582 Microphysical properties can vary significantly at the pixel level, and relying solely on average or maximum D_m and N_w values
583 captures only part of the overall process. Future work should focus on analyzing pixel-level observations to better understand
584 the characteristics of microphysical parameters within PS. Moreover, the melting layer height was not explicitly considered,
585 which limits the interpretation of vertical variations across the melting layer. Future work should incorporate pixel-level
586 observations and melting layer characteristics to better understand the microphysical features within PSs. Furthermore,
587 investigating the relationships between microphysical parameters and convective parameters will be a key focus of future
588 research. And it should also be noted that the DPR is not particularly suitable for quantifying extreme precipitation rates. In
589 heavy precipitation, Ku- and Ka-band signals are strongly affected by attenuation and multiple scattering, which can lead to
590 underestimation of radar reflectivity and the associated precipitation rates (Battaglia et al., 2014). Therefore, no further
591 discussion of extreme rain rates is provided in this study. We hope that future studies can develop improved precipitation
592 retrieval algorithms to address this issue. By analyzing the interactions between these parameters, it is possible to reveal the
593 influences of microphysical characteristics on convective intensity and precipitation patterns, providing a more detailed
594 perspective for accurately predicting and understanding precipitation phenomena.

595

596 **Data Availability.** The GPM-DPR (version 07A) data from the NASA/Goddard Space Flight Center are available at
597 https://disc.gsfc.nasa.gov/datasets/GPM_2A-DPR_07/summary. All statistics and visualization are operated with Anaconda
598 Individual Edition Python version 3.8.3 (Free Download | Anaconda, accessed on 10 April 2022).

599

600 **Author contributions.** XZ and XN conceptualised and planned the research study. XZ conducted the satellite data analysis
601 with support from XN and drafted the initial manuscript. XN and JZ reviewed and revised the manuscript to refine its content.

602

603 **Competing interests.** The contact author has declared that none of the authors has any competing interests.

604

605 **Financial support.** This study is supported by the National Natural Science Foundation of China (42105005), Fundamental
606 Research Funds for the Central Universities (SWU-KT22007), and General Program of Chongqing Natural Science
607 Foundation (2022NSCQ-MSX3145).

608

609 **References**

610 Arulraj, M. and Barros, A. P.: Automatic detection and classification of low-level orographic precipitation processes from
611 space-borne radars using machine learning, *Remote Sensing of Environment*, 257, 112355,
612 <https://doi.org/10.1016/j.rse.2021.112355>, 2021.

613 Awaka, J., Le, M., Brodzik, S., Kubota, T., Masaki, T., Chandrasekar, V., and Iguchi, T.: Development of precipitation type
614 classification algorithms for a full scan mode of GPM dual-frequency precipitation radar, *Journal of the Meteorological Society*
615 of Japan. Ser. II, 99, 1253–1270, <https://doi.org/10.2151/jmsj.2021-061>, 2021.

616 Ay, M., Özbakır, L., Kulluk, S., Gülmez, B., Öztürk, G., and Özer, S.: FC-Kmeans: Fixed-centered K-means algorithm, *Expert*
617 *Systems with Applications*, 211, 118656, <https://doi.org/10.1016/j.eswa.2022.118656>, 2023.

618 Bang, S. D. and Cecil, D. J.: Testing Passive Microwave-Based Hail Retrievals Using GPM DPR Ku-Band Radar, *Journal of*
619 *Applied Meteorology and Climatology*, 60, 255–271, <https://doi.org/10.1175/JAMC-D-20-0129.1>, 2021.

620 Battaglia, A., Tanelli, S., Heymsfield, G. M., and Tian, L.: The Dual Wavelength Ratio Knee: A Signature of Multiple
621 Scattering in Airborne Ku–Ka Observations, *Journal of Applied Meteorology and Climatology*, 53, 1790–1808,
622 <https://doi.org/10.1175/JAMC-D-13-0341.1>, 2014.

623 Becker, T. and Hohenegger, C.: Entrainment and its dependency on environmental conditions and convective organization in
624 convection-permitting simulations, *Monthly Weather Review*, 149, 537–550, <https://doi.org/10.1175/MWR-D-20-0229.1>,
625 2021.

626 Bringi, V. N., Chandrasekar, V., Hubbert, J., Gorgucci, E., Randeu, W. L., and Schoenhuber, M.: Raindrop size distribution
627 in different climatic regimes from disdrometer and dual-polarized radar analysis, *Journal of the Atmospheric Sciences*, 60,
628 354–365, [https://doi.org/10.1175/1520-0469\(2003\)060<0354:RSDIDC>2.0.CO;2](https://doi.org/10.1175/1520-0469(2003)060<0354:RSDIDC>2.0.CO;2), 2003.

629 Cha, J. W. and Yum, S. S.: Characteristics of Precipitation Particles Measured by PARSIVEL Disdrometer at a Mountain and
630 a Coastal Site in Korea, *Asia-Pacific J Atmos Sci*, 57, 261–276, <https://doi.org/10.1007/s13143-020-00190-6>, 2021.

631 Chase, R. J., Nesbitt, S. W., and McFarquhar, G. M.: Evaluation of the Microphysical Assumptions within GPM-DPR Using
632 Ground-Based Observations of Rain and Snow, *Atmosphere*, 11, 619, <https://doi.org/10.3390/atmos11060619>, 2020.

633 Chen, B. and Liu, C.: Warm organized rain systems over the tropical eastern Pacific, *Journal of Climate*, 29, 3403–3422,
634 <https://doi.org/10.1175/JCLI-D-15-0177.1>, 2016.

635 Chen, B., Hu, W., and Pu, J.: Characteristics of the raindrop size distribution for freezing precipitation observed in southern
636 China, *Journal of Geophysical Research: Atmospheres*, 116, <https://doi.org/10.1029/2010JD015305>, 2011.

637 Chudler, K., Rutledge, S. A., and Dolan, B.: Unique radar observations of large raindrops in tropical warm rain during PISTON,
638 *Monthly Weather Review*, 150, 2719–2736, <https://doi.org/10.1175/MWR-D-21-0298.1>, 2022.

639 D’Adderio, L. P., Vulpiani, G., Porcù, F., Tokay, A., and Meneghini, R.: Comparison of GPM Core Observatory and Ground-
640 Based Radar Retrieval of Mass-Weighted Mean Raindrop Diameter at Midlatitude, *Journal of Hydrometeorology*, 19, 1583–
641 1598, <https://doi.org/10.1175/JHM-D-18-0002.1>, 2018.

642 Dai, Q., Zhu, J., Zhang, S., Zhu, S., Han, D., and Lv, G.: Estimation of rainfall erosivity based on WRF-derived raindrop size
643 distributions, *Hydrology and Earth System Sciences*, 24, 5407–5422, <https://doi.org/10.5194/hess-24-5407-2020>, 2020.

644 Das, S. and Chatterjee, C.: Rain characterization based on maritime and continental origin at a tropical location, *Journal of*
645 *Atmospheric and Solar-Terrestrial Physics*, 173, 109–118, <https://doi.org/10.1016/j.jastp.2018.02.011>, 2018.

646 Das, S., Wang, Y., Gong, J., Ding, L., Munchak, S. J., Wang, C., Wu, D. L., Liao, L., Olson, W. S., and Barahona, D. O.: A
647 comprehensive machine learning study to classify precipitation type over land from Global Precipitation Measurement
648 Microwave Imager (GPM-GMI) measurements, *Remote Sensing*, 14, 3631, <https://doi.org/10.3390/rs14153631>, 2022.

649 Dolan, B., Fuchs, B., Rutledge, S. A., Barnes, E. A., and Thompson, E. J.: Primary modes of global drop size distributions,
650 *Journal of the Atmospheric Sciences*, 75, 1453–1476, <https://doi.org/10.1175/JAS-D-17-0242.1>, 2018.

651 El Khattabi, M.-Z., El Jai, M., Lahmadi, Y., Oughdir, L., and Rahhali, M.: Understanding the Interplay Between Metrics,
652 Normalization Forms, and Data distribution in K-Means Clustering: A Comparative Simulation Study, *Arab J Sci Eng*, 49,
653 2987–3007, <https://doi.org/10.1007/s13369-023-07741-9>, 2024.

654 Festa, D., Novellino, A., Hussain, E., Bateson, L., Casagli, N., Confuorto, P., Del Soldato, M., and Raspini, F.: Unsupervised
655 detection of InSAR time series patterns based on PCA and K-means clustering, *International Journal of Applied Earth*
656 *Observation and Geoinformation*, 118, 103276, <https://doi.org/10.1016/j.jag.2023.103276>, 2023.

657 Gang, A. and Bajwa, W. U.: FAST-PCA: A Fast and Exact Algorithm for Distributed Principal Component Analysis, *IEEE*
658 *Transactions on Signal Processing*, 70, 6080–6095, <https://doi.org/10.1109/TSP.2022.3229635>, 2022.

659 Gupta, A. K., Deshmukh, A., Waman, D., Patade, S., Jadav, A., Phillips, V. T. J., Bansemer, A., Martins, J. A., and Gonçalves,
660 F. L. T.: The microphysics of the warm-rain and ice crystal processes of precipitation in simulated continental convective
661 storms, *Commun Earth Environ*, 4, 226, <https://doi.org/10.1038/s43247-023-00884-5>, 2023.

662 Hamada, A., Takayabu, Y. N., Liu, C., and Zipser, E. J.: Weak linkage between the heaviest rainfall and tallest storms, *Nature*
663 *Communications*, 6, 6213, <https://doi.org/10.1038/ncomms7213>, 2015.

664 Hou, A. Y., Kakar, R. K., Neeck, S., Azarbarzin, A. A., Kummerow, C. D., Kojima, M., Oki, R., Nakamura, K., and Iguchi,
665 T.: The global precipitation measurement mission, *Bulletin of the American Meteorological Society*, 95, 701–722,
666 <https://doi.org/10.1175/BAMS-D-13-00164.1>, 2014.

667 Houze Jr., R. A., Rasmussen, K. L., Zuluaga, M. D., and Brodzik, S. R.: The variable nature of convection in the tropics and
668 subtropics: A legacy of 16 years of the Tropical Rainfall Measuring Mission satellite, *Reviews of Geophysics*, 53, 994–1021,
669 <https://doi.org/10.1002/2015RG000488>, 2015.

670 Hu, X., Ai, W., Qiao, J., and Yan, W.: Insight into global climatology of melting layer: latitudinal dependence and orographic
671 relief, *Theor Appl Climatol*, 155, 4863–4873, <https://doi.org/10.1007/s00704-024-04926-6>, 2024.

672 Iguchi, T., Kozu, T., Meneghini, R., Awaka, J., and Okamoto, K.: Rain-Profiling algorithm for the TRMM precipitation radar,
673 *Journal of Applied Meteorology and Climatology*, 39, 2038–2052, [https://doi.org/10.1175/1520-0450\(2001\)040<2038:RPAFTT>2.0.CO;2](https://doi.org/10.1175/1520-0450(2001)040<2038:RPAFTT>2.0.CO;2), 2000.

674
675 Iguchi, T., Seto, S., Meneghini, R., Yoshida, N., Awaka, J., Le, M., Chandrasekar, V., Brodzik, S., Tanelli, S., Kanemaru, K.,
676 Masaki, T., Kubota, T., and Takahashi, N.: GPM/DPR Level-2 Algorithm Theoretical Basis Document, 2021.

677 Jain, A. K.: Data clustering: 50 years beyond K-means, *Pattern Recognition Letters*, 31, 651–666,
678 <https://doi.org/10.1016/j.patrec.2009.09.011>, 2010.

679 Jiang, H.: The relationship between tropical cyclone intensity change and the strength of inner-core convection, *Monthly*
680 *Weather Review*, 140, 1164–1176, <https://doi.org/10.1175/MWR-D-11-00134.1>, 2012.

681 Jolliffe, I. T. and Cadima, J.: Principal component analysis: a review and recent developments, *Philosophical Transactions of*
682 *the Royal Society A: Mathematical, Physical and Engineering Sciences*, 374, 20150202,
683 <https://doi.org/10.1098/rsta.2015.0202>, 2016.

684 Kumar, K. S., Das, S. K., Deshpande, S. M., Deshpande, M., and Pandithurai, G.: Regional variability of precipitation
685 characteristics in tropical cyclones over the North Indian Ocean from GPM-DPR measurements, *Atmospheric Research*, 283,
686 106568, <https://doi.org/10.1016/j.atmosres.2022.106568>, 2023.

687 Kumar, S., Flores-Rojas, J. L., Moya-Álvarez, A. S., Martínez-Castro, D., and Silva, Y.: Hydrometeors distribution in intense
688 precipitating cloud cells over the earth's during two rainfall seasons, *J Indian Soc Remote Sens*, 52, 95–111,
689 <https://doi.org/10.1007/s12524-023-01805-x>, 2024.

690 Kumjian, M. R. and Prat, O. P.: The impact of raindrop collisional processes on the polarimetric radar variables, *Journal of the*
691 *Atmospheric Sciences*, 71, 3052–3067, <https://doi.org/10.1175/JAS-D-13-0357.1>, 2014.

692 Lerber, A. von, Moisseev, D., Marks, D. A., Petersen, W., Harri, A.-M., and Chandrasekar, V.: Validation of GMI Snowfall
693 Observations by Using a Combination of Weather Radar and Surface Measurements, *Journal of Applied Meteorology and*
694 *Climatology*, 57, 797–820, <https://doi.org/10.1175/JAMC-D-17-0176.1>, 2018.

695 Li, D., Qi, Y., and Li, H.: Statistical characteristics of convective and stratiform precipitation during the rainy season over
696 South China based on GPM-DPR observations, *Atmospheric Research*, 301, 107267,
697 <https://doi.org/10.1016/j.atmosres.2024.107267>, 2024.

698 Liu, C.: Rainfall Contributions from Precipitation Systems with Different Sizes, Convective Intensities, and Durations over
699 the Tropics and Subtropics, *Journal of Hydrometeorology*, 12, 394–412, <https://doi.org/10.1175/2010JHM1320.1>, 2011.

700 Liu, C. and Zipser, E. J.: The global distribution of largest, deepest, and most intense precipitation systems, *Geophysical*
701 *Research Letters*, 42, 3591–3595, <https://doi.org/10.1002/2015GL063776>, 2015.

702 Liu, C., Zipser, E. J., and Nesbitt, S. W.: Global Distribution of Tropical Deep Convection: Different Perspectives from TRMM
703 Infrared and Radar Data, <https://doi.org/10.1175/JCLI4023.1>, 2007.

704 Liu, C., Zipser, E. J., Cecil, D. J., Nesbitt, S. W., and Sherwood, S.: A cloud and precipitation feature database from nine years
705 of TRMM observations, *Journal of Applied Meteorology and Climatology*, 47, 2712–2728,
706 <https://doi.org/10.1175/2008JAMC1890.1>, 2008.

707 Liu, N., Liu, C., and Hayden, L.: Climatology and detection of overshooting convection from 4 years of GPM precipitation
708 radar and passive microwave observations, *Journal of Geophysical Research: Atmospheres*, 125, e2019JD032003,
709 <https://doi.org/10.1029/2019JD032003>, 2020.

710 Marukatat, S.: Tutorial on PCA and approximate PCA and approximate kernel PCA, *Artif Intell Rev*, 56, 5445–5477,
711 <https://doi.org/10.1007/s10462-022-10297-z>, 2023.

712 Marzuki, M., Ramadhan, R., Yusnaini, H., Renggono, F., Vonnisa, M., and Hashiguchi, H.: Comparison of vertical profile of
713 raindrop size distribution from micro rain radar with global precipitation measurement over Western Java Island, *Remote*
714 *Sensing Applications: Society and Environment*, 29, 100885, <https://doi.org/10.1016/j.rsase.2022.100885>, 2023.

715 Mroz, K., Battaglia, A., and Fridlind, A. M.: Enhancing consistency of microphysical properties of precipitation across the
716 melting layer in dual-frequency precipitation radar data, *Atmospheric Measurement Techniques*, 17, 1577–1597,
717 <https://doi.org/10.5194/amt-17-1577-2024>, 2024.

718 Ni, X., Liu, C., Cecil, D. J., and Zhang, Q.: On the detection of hail Using satellite passive microwave radiometers and
719 precipitation radar, *Journal of Applied Meteorology and Climatology*, 56, 2693–2709, <https://doi.org/10.1175/JAMC-D-17->
720 0065.1, 2017.

721 Ni, X., Liu, C., and Zipser, E.: Ice microphysical properties near the tops of deep convective cores implied by the GPM Dual-
722 Frequency Radar observations, *Journal of the Atmospheric Sciences*, 76, 2899–2917, <https://doi.org/10.1175/JAS-D-18->
723 0243.1, 2019.

724 Peinó, E., Bech, J., Polls, F., Udina, M., Petracca, M., Adirosi, E., Gonzalez, S., and Boudevillain, B.: Validation of GPM DPR
725 Rainfall and Drop Size Distributions Using Disdrometer Observations in the Western Mediterranean, *Remote Sensing*, 16,
726 2594, <https://doi.org/10.3390/rs16142594>, 2024.

727 Roy, P., Biswasharma, R., Deshamukhya, A., and Sharma, S.: Spatial and seasonal variation of rainfall contribution by the
728 height spectrum of precipitation systems and associated cloud bulk properties over the South Asia, *International Journal of*
729 *Climatology*, 40, 3771–3791, <https://doi.org/10.1002/joc.6427>, 2020.

730 Ryu, J., Song, H.-J., Sohn, B.-J., and Liu, C.: Global distribution of three types of drop size distribution representing heavy
731 rainfall from GPM/DPR measurements, *Geophysical Research Letters*, 48, e2020GL090871,
732 <https://doi.org/10.1029/2020GL090871>, 2021.

733 Saha, P., Majumder, S., and Maitra, A.: Rain drop size distribution analysis at a tropical location near land-sea boundary,
734 *Theor Appl Climatol*, 147, 487–498, <https://doi.org/10.1007/s00704-021-03809-4>, 2022.

735 Seela, B. K., Janapati, J., Lin, P.-L., Wang, P. K., and Lee, M.-T.: Raindrop size distribution characteristics of summer and
736 winter season rainfall over North Taiwan, *Journal of Geophysical Research: Atmospheres*, 123, 11,602–11,624,
737 <https://doi.org/10.1029/2018JD028307>, 2018.

738 Shi, R., Lu, C., Xu, W., and Luo, Y.: A global view on microphysical discriminations between heavier and lighter convective
739 rainfall, *Commun Earth Environ*, 6, 511, <https://doi.org/10.1038/s43247-025-02473-0>, 2025.

740 Skofronick-Jackson, G., Petersen, W. A., Berg, W., Kidd, C., Stocker, E. F., Kirschbaum, D. B., Kakar, R., Braun, S. A.,
741 Huffman, G. J., Iguchi, T., Kirstetter, P. E., Kummerow, C., Meneghini, R., Oki, R., Olson, W. S., Takayabu, Y. N., Furukawa,
742 K., and Wilheit, T.: The global precipitation measurement (GPM) mission for science and society, *Bulletin of the American*
743 *Meteorological Society*, 98, 1679–1695, <https://doi.org/10.1175/BAMS-D-15-00306.1>, 2017.

744 Snook, N. and Xue, M.: Effects of microphysical drop size distribution on tornadogenesis in supercell thunderstorms,
745 *Geophysical Research Letters*, 35, <https://doi.org/10.1029/2008GL035866>, 2008.

746 Sowan, B., Hong, T.-P., Al-Qerem, A., Alauthman, M., and Matar, N.: Ensembling validation indices to estimate the optimal
747 number of clusters, *Appl Intell*, 53, 9933–9957, <https://doi.org/10.1007/s10489-022-03939-w>, 2023.

748 Suh, S.-H., You, C.-H., and Lee, D.-I.: Climatological characteristics of raindrop size distributions in Busan, Republic of Korea,
749 *Hydrology and Earth System Sciences*, 20, 193–207, <https://doi.org/10.5194/hess-20-193-2016>, 2016.

750 Sun, Y., Dong, X., Cui, W., Zhou, Z., Fu, Z., Zhou, L., Deng, Y., and Cui, C.: Vertical Structures of Typical Meiyu
751 Precipitation Events Retrieved From GPM-DPR, *Journal of Geophysical Research: Atmospheres*, 125, e2019JD031466,
752 <https://doi.org/10.1029/2019JD031466>, 2020.

753 Tapiador, F. J., Turk, F. J., Petersen, W., Hou, A. Y., García-Ortega, E., Machado, L. A. T., Angelis, C. F., Salio, P., Kidd, C.,
754 Huffman, G. J., and de Castro, M.: Global precipitation measurement: Methods, datasets and applications, *Atmospheric*
755 *Research*, 104–105, 70–97, <https://doi.org/10.1016/j.atmosres.2011.10.021>, 2012.

756 Thompson, E. J., Rutledge, S. A., Dolan, B., and Thurai, M.: Drop size distributions and radar observations of convective and
757 stratiform rain over the equatorial Indian and west Pacific Oceans, *Journal of the Atmospheric Sciences*, 72, 4091–4125,
758 <https://doi.org/10.1175/JAS-D-14-0206.1>, 2015.

759 Uma, K. N. and Rao, T. N.: Characteristics of vertical velocity cores in different convective systems observed over Gadanki,
760 India, *Monthly Weather Review*, 137, 954–975, <https://doi.org/10.1175/2008MWR2677.1>, 2009.

761 Wang, T. and Tang, G.: Spatial Variability and Linkage Between Extreme Convections and Extreme Precipitation Revealed
762 by 22-Year Space-Borne Precipitation Radar Data, *Geophysical Research Letters*, 47, e2020GL088437,
763 <https://doi.org/10.1029/2020GL088437>, 2020.

764 Wen, J., Wang, G., Zhou, R., Li, R., Zhaxi, S., and Bai, M.: Seasonal Variation in Vertical Structure for Stratiform Rain at
765 Médog Site in Southeastern Tibetan Plateau, *Remote Sensing*, 16, 1230, <https://doi.org/10.3390/rs16071230>, 2024.

766 Wen, L., Chen, G., Yang, C., Zhang, H., and Fu, Z.: Seasonal variations in precipitation microphysics over East China based
767 on GPM DPR observations, *Atmospheric Research*, 293, 106933, <https://doi.org/10.1016/j.atmosres.2023.106933>, 2023.

768 Wu, Z., Zhang, Y., Zhang, L., Zheng, H., and Huang, X.: A comparison of convective and stratiform precipitation microphysics
769 of the record-breaking typhoon In-Fa (2021), *Remote Sensing*, 14, 344, <https://doi.org/10.3390/rs14020344>, 2022.

770 Zhang, Y. and Wang, K.: Global precipitation system size, *Environ. Res. Lett.*, 16, 054005, [https://doi.org/10.1088/1748-](https://doi.org/10.1088/1748-9326/abf394)
771 [9326/abf394](https://doi.org/10.1088/1748-9326/abf394), 2021.

772 Zhang, Z., Li, H., Li, D., and Qi, Y.: Spatial variability of raindrop size distribution at Beijing city scale and its implications
773 for polarimetric radar QPE, *Remote Sensing*, 15, 3964, <https://doi.org/10.3390/rs15163964>, 2023.

774 Zipser, E. J., Cecil, D. J., Liu, C., Nesbitt, S. W., and Yorty, D. P.: WHERE ARE THE MOST INTENSE THUNDERSTORMS
775 ON EARTH?, *Bull. Amer. Meteor. Soc.*, 87, 1057–1072, <https://doi.org/10.1175/BAMS-87-8-1057>, 2006.

776